SAHLGRENSKA ACADEMY
DEPARTMENT OF MEDICAL RADIATION SCIENCES

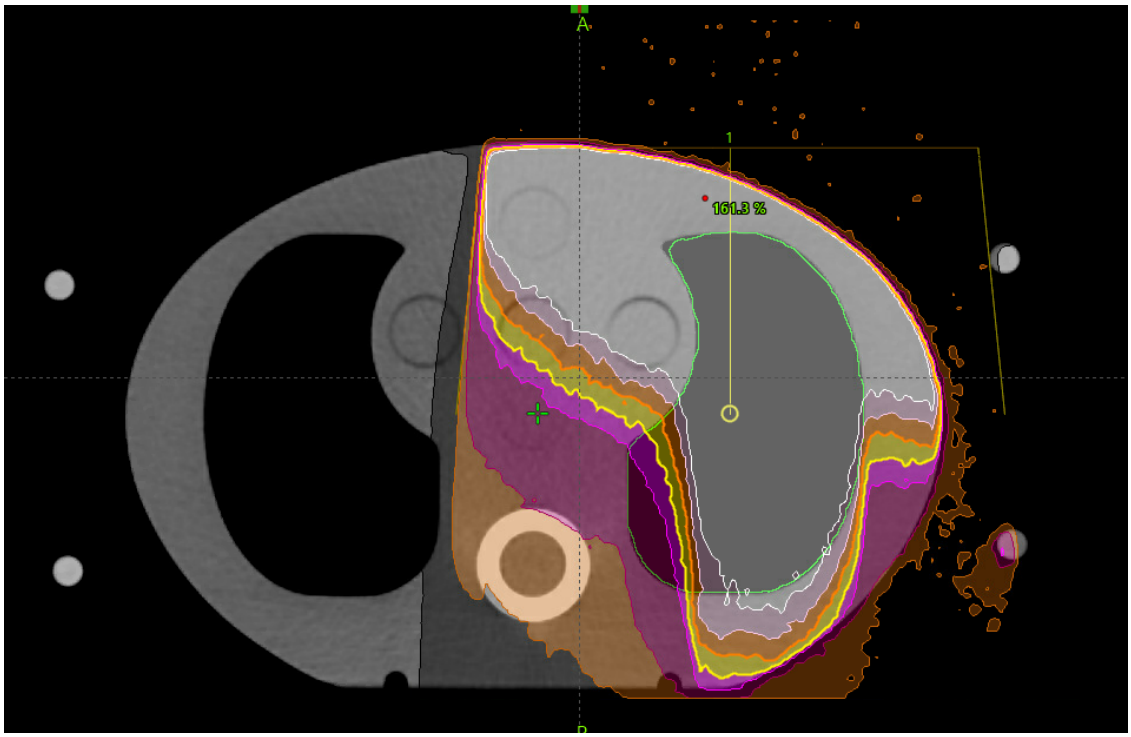

Monte Carlo evaluation of static and dynamic 6FFF treatments

Evaluation of dose distributions calculated with AAA, Acuros XB, and Collapsed Cone (RayStation and DoseCheck)

Alma Blombäck

Essay/Thesis:	30 hp
Program:	Medical physics
Level:	Second cycle
Term/year:	Autumn 2022
Supervisors:	Roumiana Chakarova, Marcus Krantz
Examiner:	Magnus Båth

MASTER'S THESIS 2023

Monte Carlo evaluation of static and dynamic 6FFF treatments

Evaluation of dose distributions calculated with AAA, Acuros XB, and Collapsed Cone (RayStation and DoseCheck)

Alma Blombäck

UNIVERSITY OF GOTHENBURG

Department of Medical Radiation Sciences
UNIVERSITY OF GOTHENBURG
Gothenburg, Sweden 2023

Monte Carlo evaluation of static and dynamic 6FFF treatments
Alma Blombäck

Supervisor: Roumiana Chakarova, Marcus Krantz
Examiner: Magnus Båth

Master's Thesis 2023
Department of Medical Radiation Sciences
University of Gothenburg

Cover: A lung phantom with a 6FFF Monte Carlo calculated dose distribution.

Typeset in LaTeX
Gothenburg, Sweden 2023

Essay/Thesis:	30 hp
Program:	Medical physics
Level:	Second cycle
Term/year:	Autumn 2022
Supervisors:	Roumiana Chakarova, Marcus Krantz
Examiner:	Magnus Båth
Keywords:	Monte Carlo, 6FFF, flattening filter free, AAA, Acuros XB, DoseCheck, RayStation, DVH evaluation

Abstract

There are several benefits to removing the standard flattening filter and using so-called flattening filter free (FFF) treatments in external radiation therapy with photons. The main advantage is the possibility of significantly shortening the treatment time, despite this FFF is not widely used yet. This thesis evaluates static and dynamic 6FFF dose distributions calculated with algorithms AAA, Acuros XB, and two implementations of Collapsed Cone (RayStation, and DoseCheck) with Monte Carlo calculations. A Monte Carlo 6FFF accelerator model was first validated in a water phantom and a previously developed Monte Carlo system was calibrated for 6FFF. Eight clinically planned patient plans, including prostate plans, brain plans, and plans in the thorax region, as well as one lung phantom plan were recalculated with all algorithms. The resulting dose distributions were then evaluated against Monte Carlo using DVH evaluations. It was found that Acuros XB had the best agreement with Monte Carlo followed by AAA, both algorithms having a comparable agreement as previously evaluated 6X plans. DoseCheck's implementation of Collapsed Cone was found to underestimate the dose and RayStation's differed the most from Monte Carlo. In conclusion, this study suggests that dose distributions calculated with AAA and Acuros XB do not lose accuracy when the flattening filter is removed. Further, the algorithms used in DoseCheck and Raystations should be more investigated.

Sammanfattning

Det finns flera fördelar med att ta bort utjämningsfiltret som annars är standard och använda så kallade FFF-behandlingar vid extern strålbehandling med fotoner. Den största fördelen är möjligheten att avsevärt förkorta behandlingstiden, trots detta är användningen av FFF ännu inte utbredd. I detta arbete utvärderades statiska och dynamiska 6FFF-dosfördelningar beräknade med algoritmerna AAA, Acuros XB, och två implementationer av Collapsed Cone (RayStation och DoseCheck) med Monte Carlo. Först gjordes en validering av en Monte Carlo 6FFF acceleratormodell i ett vattenfantom och ett tidigare utvecklat Monte Carlo system kalibrerades för 6FFF. Åtta kliniskt planerade patientplaner, inkluderat prostataplaner, hjärnplaner och planer i toraxregionen, samt en lungfantomplan beräknades med samtliga algoritmer. De resulterade dosfördelningarna utvärderades mot Monte Carlo fördelningen med DVH-utvärderingar. Resultatet visade att Acuros XB överensstämde mest med Monte Carlo följt av AAA, båda algoritmerna hade jämförbara överensstämmelser som tidigare utvärderade 6X planer. Utvärderingen av DoseChecks implementation av Collapsed Cone visade på en underestimering av dosen och sämst överensstämmelse med Monte Carlo hade RayStations implementation. Sammanfattningsvis visar detta arbete på att dosfördelningar beräknade med AAA och Acuros XB inte förlorar noggrannhet när utjämningsfiltret tas bort. Vidare bör algoritmerna som används i DoseCheck och Raystations undersökas ytterligare.

Acknowledgements

An enormus thanks to my head supervisor Roumiana Chakarova for guiding and supporting me throughout this work, non of it would be possible without you. I would also like to thank my co-supervisor Marcus Krantz for his guidance and Eric Grönlund for learning me the basics of RayStation. A thanks also goes out to Niclas Pettersson, who helped with Eclipse Research module as well as with validation of CT curves. My greatest appreciation also goes out to everyone in the department who found FFF plans to evaluate or supported this work in other ways.

Finally I would like to thank Oliver and my family for giving me endless support in all things I dare embark upon. ♡

Alma Blombäck, Gothenburg, February 2023

Contents

List of Acronyms

Below is the list of acronyms that have been used throughout this thesis listed in alphabetical order:

AAA	Analytical Anisotropic Algorithm
AXB	Acuros XB
CC	Collapsed Cone
CTV	Clinical Target Volume
DC	DoseCheck
DICOM	Digital Imaging and Communications in Medicine
FFF	Flattening Filter Free
GTV	Gross Tumor Volume
IC	Ionizing Chamber
IMRT	Intensity Modulated Radiation Therapy
linac	Linear Accelerator
MC	Monte Carlo
MLC	Multi-Leaf Collimator
MU	Monitor Unit
MV	Megavolt
OAR	Organ At Risk
PB	Pencil Beam
PDD	Percentage Depth Dose
PTV	Planning Target Volume
RS	RayStation
SBRT	Stereotactic Body Radiation Therapy
SC	Spinal Cord
SRS	Stereotactic Radiosurgery
SSD	Source to Surface Distance
TPS	Treatment Planning System
VMAT	Volumetric Modulated Arc Therapy
WBRT	Whole Brain Radiation Therapy
6FFF	Energy 6 MV and Flattening Filter Free
6X	Energy 6 MV with Flattening Filter

1

Introduction

Currently, radiation therapy is used to treat many different forms of cancer and it is estimated that around 50% of Swedish cancer patients are recommended radiation therapy during some stage of their treatment [1]. During the last few years, there has been a rapid development in radiation treatments due to the introduction of new technologies, made possible by the increased availability of computer power [1]. There are various types of radiation therapy which are classified according to if the source is placed externally, outside off, or internally, inside off, the patient. This work will concern external radiation therapy with photons.

In radiation therapy, ionizing radiation is used to cause single- and double-strand breaks in the DNA to induce irreparable DNA damage in the cancerous cells. This DNA damage is a result of the particles interacting with the matter and releasing energy. To quantify the released energy the unit gray (Gy) is used, which is defined as the absorbed energy deposited in a medium subjected to radiation per unit mass [2], called the absorbed dose, in this thesis referred to as the dose. In external radiation therapy with photons, a linear accelerator (linac) is used to produce the radiation. The linac produces photon beams by accelerating electrons towards a high-density target. The resulting photon beam is polyenergetic and denoted by the electron energy used to create it but with unit MV (Megavolt). Clinical linacs typically produce photon beams with energies ranging from 4 to 24 MV [2].

The linac can deliver the radiation either statically or dynamically. In static treatments, all parameters such as the angle of the linac and the position of the radiation collimators are kept constant during the radiation. These parameters can then be changed to the next position in the plan, in other words, every parameter is static when the radiation is delivered. In dynamic treatments, one or multiple parameters are changed during the radiation delivery. A common type of dynamic treatment is the VMAT technique (volumetric modulated arc therapy) which enables dynamic multi-leaf collimators (MLC), gantry speed, and dose rate to be used to create case-specific field shapes.

To treat cancer effectively the gold rule of radiation therapy is to deliver the right dose to the right place. That is to maximize the dose delivered to the cancerous cells while also minimizing the absorbed dose to surrounding tissue as well as being sure that this maximization and minimization take place in the right place. These aims of maximization and minimization contradict and lead to a constant trade-off. Research in

radiation therapy is often done to decrease this trade-off or optimize the accuracy of the dose placement.

One way of optimizing the treatments is to minimize the uncertainty of the patient's movements during the radiation delivery. This can be done by example asking the patient to hold their breath or fixating the patient to the treatment table. An additional way to minimize the movement of the patient, as well as internal organ movement, is to deliver the dose quicker, which can be done by increasing the intensity of the beam, achieving a higher dose rate.

When producing the photon beam used for treatment the standard is to let the photons pass through a cone-shaped filter called flattening filter. The filter is usually made of a material with a high atomic number such as tungsten, iron, or copper, and is used to even out the lateral intensity distribution because the angular distribution of the primary photons is predominantly in the forward direction [1]. Although useful in some situations the flattening filter is no longer necessary as the calculation algorithms used to estimate the radiation delivered to the patient can now take into account the unevenness of the beam intensity. By removing the filter and creating beams called flattening filter free (FFF) the intensity of the beam can be increased by 2-4 times, which in turn can shorten the treatment time significantly resulting in less risk of movement during treatment [1]. Another benefit of removing the flattening filter is a reduction of scattered photons in the filter reducing the out-off-field dose to the patient [1].

Previous studies have been done to examine the quality of treatments given with FFF photon beams and concluded no decrease in effectiveness. The study ref. [3] compared FFF therapy for lung stereotactic body radiotherapy (SBRT) with FF therapy and found that FFF treatments entail both shorter treatment times and a maintained low toxicity and high local control. Similar results can be seen for brain treatments and prostate treatment as in ref. [4] it was found that FFF VMAT whole brain radiotherapy offered more hippocampal sparing and in ref. [5] the removal of the flattening filter did not reduce the quality of the prostate treatment and the treatment time was halved. A commercial linear accelerator from Varian, "TrueBeam", was made available on the market in 2010, and since many clinics have the option of treating with FFF [1]. To ensure that no reduction in efficiency occurs when the flattening filter is removed, it is important to ensure that the calculation algorithms used to calculate the dose to the patient during treatment planning handle FFF energies correctly.

When treatment planning a dose distribution in the patient geometry is calculated so that the plan can be optimized and it can be ensured that the target gets the prescribed dose and that the dose constraints given for the organs at risk (OAR) and surrounding tissue are not exceeded [2]. When calculating dose distributions, the algorithms used must not only be fast, to not disrupt the patient flow in the clinic, but also accurate[2]. Various algorithms can be applied all of which have advantages and disadvantages. Some developed to be fast, some to be accurate and some to be both. At Sahlgrenska University hospital several calculation algorithms and a Monte Carlo (MC) method is of relevance. Hence, a thorough evaluation of FFF dose distributions calculated with different dose distribution calculating algorithms is a necessity. The algo-

rithms in use at Sahlgrenska University hospital is the analytical anisotropic algorithm (AAA), Acuros XB (AXB) and two implementations of Collapsed Cone (CC); RayStation (RS) and DoseCheck (DC).

1.1 Aim

This thesis aims to evaluate static and dynamic 6FFF dose distributions calculated by AAA, AXB, and two implementations of CC (RS and DC) with an MC method in phantom and patient geometry. The thesis is divided into two parts: a validation of the Monte Carlo 6FFF accelerator model in a water phantom and an evaluation of the 6FFF dose distributions in a heterogeneous phantom and patient geometry.

2

Theory

This chapter is divided into two sections. The first section discussing the production, evaluation and characteristics of FFF beams. The second section contains a description of the algorithms Analytical Anisotropic Algorithm (AAA), Collapsed Cone (CC), Acurox XB (AXB) and Monte Carlo (MC).

2.1 Producing and Evaluating Flattening Filter Free beams

Radiotherapy used for the treatment of cancer started after the discovery of X-rays 1896 [6]. In the beginning, the treatments were carried out using X-ray machines. In the 1950 machines using Cobalt-60 and linear accelerators were introduced and have been used mainly since then [6]. The popularity of the linear accelerator exceeds the Cobalt-60 machine as it has a wider range of photon energies and does not include the handling of radioactive sources.

It has been the standard to equip linear accelerators with flattening filter since the 1950, but research on the benefits of there removal has been conducted since the 80's [1]. The company Varian released their linear accelerator called TrueBeam with a flattening filter free option in 2010 [1] and since then many clinics have gained the possibly of treating patients with FFF photon beams.

2.1.1 Components of a Linear Accelerator

The linear accelerator (linac) is the most common equipment used to produce radiation for external treatments with photons and electrons [7]. Different types of linacs vary in appearance and components but generally function in the same way. In this thesis, the components used to produce photon beams are discussed.

The main features of the linac are a treatment couch where the patient is placed during treatment, a stand, and a gantry containing the devices used to produce the beams [7]. The gantry is connected to the stand, which is fixed, and enables the gantry to rotate 360°around the treatment couch [7]. The main components contained in the gantry are shown in figure 2.1, which are an electron stand, accelerating waveguide, bending magnets, target, primary collimators, flattening filter, ionizing chamber, jaws, and MLC.

The part of the gantry that includes the collimators and flattening filter, marked in figure 2.1 with a light blue, is called the accelerator head. It is the accelerator head that is modeled in MC accelerator modeling, along with the electron beam hitting the target. The properties of the electron beam, target, and flattening filter differ with different energy modes which is why different MC accelerator models are used for different energies. Primary collimators, jaws, and MLC are modeled the same for all energies.

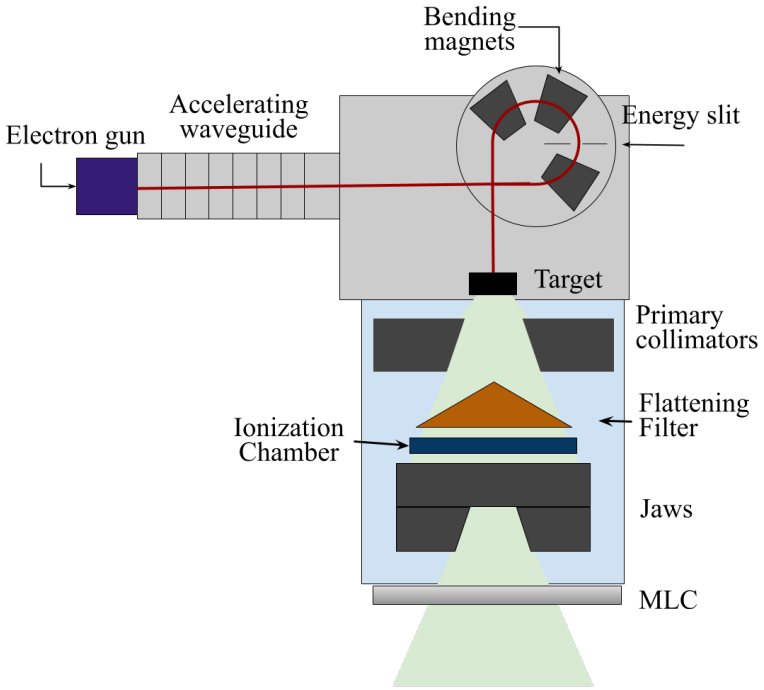

Figure 2.1: Schematic overview of the main components in the linac gantry.

The electron gun consists of an anode and cathode, and an electron beam is produced by heating the cathode releasing electrons, and then letting these electrons accelerate towards the anode [7]. The anode contains an opening letting the electrons through to the waveguide. The accelerating waveguide consisted of a hollow pipe divided into cavities and is used to accelerate the electrons. Microwaves are traveling through the waveguide, accelerating the electrons by capturing and bunching up the electrons on the moving electrical field. There are two types of accelerator waveguides: traveling and standing. The fundamental difference between the two is that in the traveling waveguide, the remaining power of the microwave is absorbed in the end of the guide while in the standing waveguide, the wave is instead reflected at the end. To provide amplified microwaves for the waveguide either a klystron amplifier or a magnetron generator is used [7].

The waveguides used are often too long to be placed vertically in the gantry and are instead placed horizontally [7]. This placement means that the electron beam must be bent 90°. Often a 270°bend is done with bending magnets, see figure 2.1. The reason

for the 270°bend is that the electron beam can be refocused to maintain a small virtual beam source size and an energy slit is used to remove electrons not within a 5% of the peak energy [7].

To convert the narrow electron beam the electrons hit a target and photons are produced via bremsstrahlung production [7]. The resulting photon beam is then collimated by the fixed primary collimators. The beam then passes through a cone-shaped flattening filter to create a uniform beam, see figure 2.1. The flattening filter is mounted on a carousel which enables the filter to be swithed out for different filters depending on energy, removed or swithed for electron scattering foils when electron treatments are performed. To monitor the symmetry, flatness, and dose output of the field produced an ionizing chamber is used. The chamber measured dose in monitor units (MU) which are calibrated so that a certain number of MU gives 1 Gy at a reference point.

Finally, the photon beam is collimated to fit the specific treatment plan. This is done by using a set of secondary collimators, called jaws, and most often multi-leaf collimators, MLC. The jaws are usually made of tungsten or lead and consist of two pairs of blocks. One pair controls the field size in the x-led and the other pairs in the y-led. The MLC consists of multiple interleaved collimators that can be individually moved to create a customized field shape, see figure 2.2.

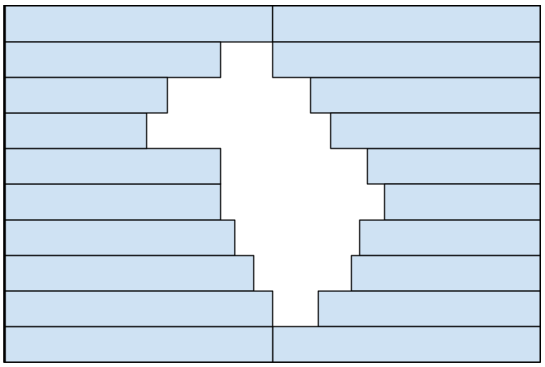

Figure 2.2: Schematic figure of the MLC used in a linac to produce patient-specific field shapes.

2.1.2 Evaluating Dose Distributions

Dose distributions, the energy deposition in the irradiated volume, can be evaluated in different ways depending on what aspects of the distribution are of interest. When evaluating one-field distributions often the dose is measured along horizontal and vertical lines. The dose measured in horizontal lines, orthogonal to the field direction, is called profiles and the dose in vertical lines, along the field direction, is called depth dose curves. These profiles and depth dose curves can both be taken from calculated dose distributions and measured in water phantoms.

In figure 2.3 a typical dose profile can be seen. Profiles can be taken at different depths, points along the z-axis, and along the x-, y-axis, or diagonally. The outer part of the profiles where the dose increases from 20% to 80% is called the penumbra, see figure 2.3. A depth dose curve is typically taken along the central axis in the field direction and plotted against the depth of the phantom. The depth at which the dose is the highest is called dose max, D_{max}. The dose can be normalized to 100% at a certain depth, D_{max} or a reference depth, the curve is then called a percentage depth dose (PDD) curve.

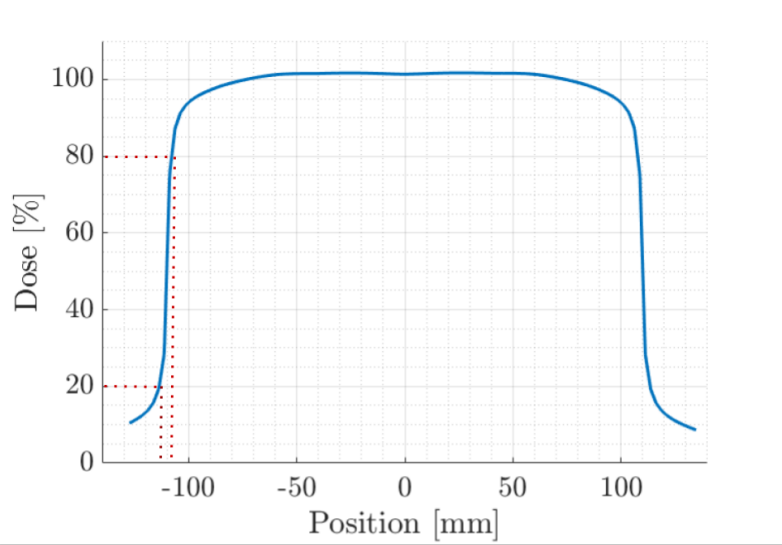

Figure 2.3: Example of a profile in water at 10 cm depth with the relative dose on the y-axis and the position along the in x-led on the x-axis. Position "0" corresponds to the beam axis (CAX). The red dotted line marks the penumbra.

When a flattening filter is used the profiles are flattened, compared to when removed, see example in figure 2.4. Aside from evening out the profiles and decreasing the intensity the flattening filter also creates scattered photons increasing the out-of-field dose received by the patient [1]. A big portion of the contamination electrons are filtered out in the flattening filter and to not lose this effect when removing it many linacs use a replacement filter usually made from a thin foil of metal [1]. The TrueBeam linac uses a 0.8 mm brass foil. As these foils are not as thick as the flattening filter they do filter out a majority of the electrons and provide a slight beam hardening effect [1]. The beam hardening effect of the flattening filter is however larger which leads to steeper dose fall-offs at depths beyond D_{max} for FFF beams [1]. The depth dose curve of a 6FFF beam with the same accelerating potential as a conventional 6 MV beam will generally correspond to a 4-5 MV beam [1]. Some producers of linacs provide a tuning of the accelerating potential to compensate for this, the TrueBeam does not.

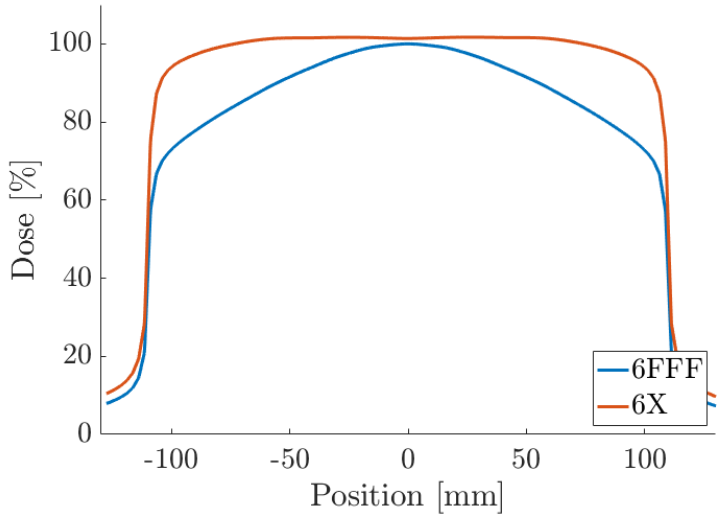

Figure 2.4: Profiles produced with, 6X, and without, 6FFF, the flattening filter with energy 6 MV.

A common way to evaluate dose distributions in treatment plans is to use a cumulative dose volume histogram (DVH), in which the volume or percentage of the total organ volume that receives what dose is presented [7]. Structures containing the tumor, often called target, important organs, for example, lung and heart are drawn on the patient images. DVH then shows what percentage of these structures receive which dose. An example of a DVH graph is presented in figure 2.5. When planning and evaluating a plan different dose and volume objectives as well as constraints that can be read out from the DVH is used to ensure that the target receives the appropriate dose and OAR is speared. Objectives and constraints specify how large a volume we want to receive a certain dose, for example, the notation $D_{98\%}$ = 60 Gy means that 98% of the volume receives 60 Gy. It can also specify how large a volume we want to have a certain dose, for example, $V_{40\,\mathrm{Gy}}$ = 50% means that we want 50% of the volume to have a dose of 40 Gy.

A so-called gamma evaluation can be done to directly compare two dose distributions. The gamma evaluation takes two aspects into account, the dose difference and the spatial difference of the distributions [8]. A gamma pass rate can also be calculated as the percentage of the points that meets predetermined requirements for dose and spatial differences [8].

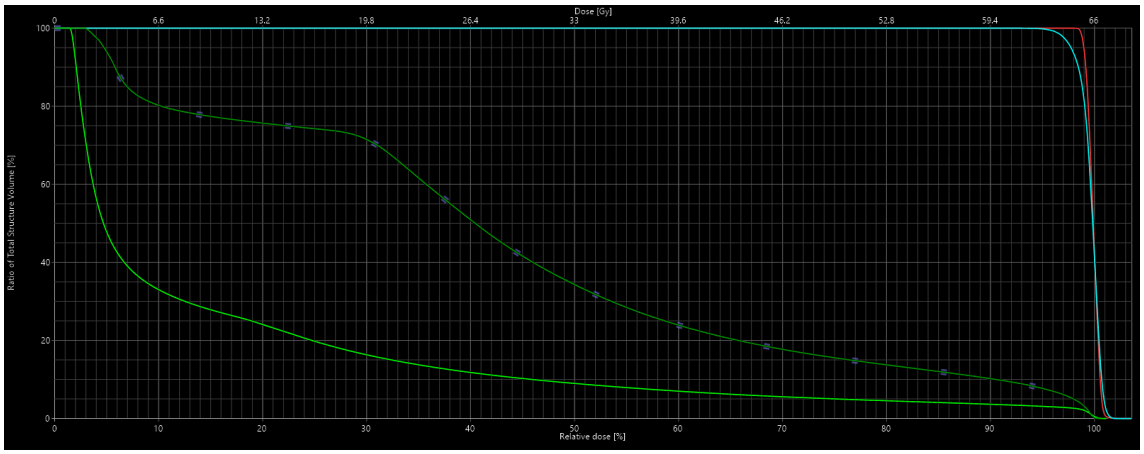

Figure 2.5: Example of a DVH for a prostate plan with the percent of the structure's volume on the y-axis and the relative dose on the x-axis. Each line represents the dose distribution in one structure. The steep curves at the upper right are structures related to the target and the other curves to the lower left are structures related to the risk organs rectum and bladder.

2.2 Dose Distribution Calculation Algorithms

Dose distribution calculation algorithms are used to make both static and dynamic plans. The accuracy of such an algorithm depends on the algorithm's ability to handle tissue heterogeneity and charge particle disequilibrium. There is currently no good way to measure the dose distribution in a patient during the treatment delivery, which makes the reliability the accuracy of distribution calculation algorithms vital for effective cancer treatments.

At present time there are several different dose calculation algorithms under constant development, all with advantages and disadvantages. Usually, dose distribution algorithms are divided into type-a and type-b according to how they account for heterogeneity. Type-a algorithms only correct for inhomogeneities vertically along the ray direction while type-b algorithms also correct laterally. The algorithms used in this thesis include AAA which is currently used clinically in treatment planning system (TPS) Eclipse at Sahlgrenska University Hospital and two CC algorithms from TPS RS and DC. These algorithms are all considered type-b algorithms and use a convolution-superposition method.

Algorithms such as AXB in Eclipse are classified as grid-based Boltzmann solvers and by many considered as the next-generation algorithms. AXB is currently under clinical implementation and is expected to replace AAA in the near future. Grid-based Boltzmann solvers function by explicitly solving the linear Boltzmann transport equation and in doing so can take heterogeneity in all directions directly into account. Algorithms based on an MC simulation of particle transport are regarded as the most accurate to date. To get statistically viable results a large number of particles has to be transported which makes these algorithms slow and are mostly regarded as too slow to use in a clinical setting.

To take the patient's or phantom's specific appearance and heterogeneities into account, all algorithms use information from computer tomography (CT) images. A calibration curve is used to translate the CT images hounsfield units into electron density or to classify the voxels as different materials. Algorithms such as AAA exclusively use electron density to account for heterogeneities, which can be seen as transporting particles and calculating the dose in water with varying electron density as opposed to in the specific mediums. These algorithms are said to present the dose as dose-to-water [9].

AXB and MC do instead classify each voxel consisting of predefined mediums, this enables these algorithms to transport the particles and calculate the dose in different mediums presenting the dose as dose-to-medium. These algorithms can also present the dose as dose-to-water by using the originally calculated dose-to-medium and converting this to dose-to-water [9]. This can be seen as assuming the voxel as a Bragg-Gray cavity of water surrounded by medium, which differs from the dose-to-water produced for example the AAA [9]. Some algorithms, for example, the CC algorithm implemented by DC uses the medium and electron density when correcting in different steps of the calculation and can be considered as a mix of dose-to-water and

dose-to-medium.

2.2.1 Monte Carlo - MC

Monte Carlo simulations are based on using random number sampling to solve macroscopic problems by simulating microscopic interactions [1]. When MC is used in the context of radiation, it involves simulating the transport of each particle through the patient or phantom geometry as well as the particle's scattering and energy deposition based on tabulated cross-sectional data [9]. The patient or phantom geometry is divided into voxels and by tracking the energy deposited in each voxel average out over a large number of traced particles the dose distribution is achieved [9].

For high-energy photons, analog particle transport, often called collision-by-collision transport is generally used [10]. Collision-by-collision is based on stimulating every interaction photons undergo as it is transported through the medium [10]. By selection from a distribution characterized as the photon's mean free pathlength, which depends on the energy of the particle and properties of the medium, the distance to the next interaction site is determined [7]. The interaction type in interaction site is based on probability. The four interaction types used are photoelectric absorption, Rayleigh scatter, Compton scatter, and pair production. The simulation steps of each particle, and eventual secondary particles created, are repeated until the particle has left the region of interest or has reached a predetermined energy, PCUT for photons and ECUT for electrons, and the energy can be assumed to be deposited locally [10]. Energies AP and AE for photons and electrons respectively are also set as cutoff energies for secondary particle production. If the particle's energy is below AP/AE a continuous slowing-down approximation can be used, which makes the calculations faster.

Theoretically, analog particle transport can be used for all particle types but in practice, it is very ineffective when simulating charged particles such as electrons [10]. This is because of the short mean free path and the huge number of interactions that charged particles go through during transportation [10]. Luckily almost all charged particle interactions are elastic or semi-elastic, that is in almost all interactions the particle loses little to no energy and the direction stays approximately the same [10]. Therefore, to efficiently simulate the transport of these particles, a condensed history (CH) technique can be used, first introduced by M. Berger in 1963 [11]. The condensed history technique is based on grouping together a large number of individual interactions into a single step [1]. After each CH step probability distributions based on multiple scatter theories are used to sample the particle's energy loss and angular deflection [1].

To model the source, MC usually uses a so-called phase space. A phase space can be seen as a virtual plan with information about the source particles position, energy and direction [10].

In this thesis the Electron-Gamma-Shower, EGSnrc [12], MC code was used for the MC dose distribution calculations together with the EGSnrc simulation systems BEAMnrc and DOSXYZnrc. To calculate MC dose distributions based on plans created in the TPS Eclipse a previously developed MC system was used. This system is based on the

EGSnrc code and was previously used in the clinic as a pre-treatment quality assurance (QA). The system works by importing the plan and CT images in DICOM (digital imaging and communications in medicine) format then recalculates the dose distributions and creates new DICOM files that can be imported back to Eclipse for evaluation.

To identify the different mediums in the patient or phantom geometry EGSnrc each voxel is assigned a medium based on the HU value of the CT images [9]. This enables the algorithm to use the cross-section data based on the voxel medium and therefore transport and calculate the dose as dose-to-medium [9]. When presenting the dose as dose-to-water the algorithm converts the calculated dose-to-medium by multiplying with the average ratio of the restricted mass electronic stopping power of water with that of the medium, yielding a dose calculated in water with varying electron density. It should be noted that particle transportation is still done in the medium.

2.2.2 Fundamentals of the Convolution/Superposition Methods

Convolution/Superposition algorithms encompass various algorithms, among these algorithms AAA and CC. They are all built on the same fundamental ideas which will be discussed in this section.

These methods for calculating dose distributions are based on dividing the radiation into interactions of primary photons and energy deposited about a primary photon interaction site [7]. The energy or dose deposited by the primary photons is calculated using the total energy released per unit mass (TERMA) [7]. The TERMA at a point $\vec{r}$ can be calculated by

$$T(\vec{r}) = \frac{\mu}{\rho}(\vec{r})\Psi(\vec{r}), \tag{2.1}$$

where $\Psi(r)$ is the fluence of primary photons at point r, μ the linear attenuation coefficient and ρ the density [7]. To calculate the TERMA when Ψ is known at a surface point r_0, $\Psi(r)$ is exponentially attenuated and for a divergent beam the inverse-square fall off is taken into account, which gives the equation [7]

$$T(\vec{r}) = \left(\frac{|\vec{r}_0|}{|\vec{r}|}\right)^2 \Psi(\vec{r}_0) e^{-\mu|\vec{r}-\vec{r}_0|\left(\frac{\mu}{\rho}\right)} \tag{2.2}$$

The distance $|\vec{r} - r_0|$ is called the geometric depth, which can be used in homogeneous mediums. To take inhomogeneities into account a radiological depth is instead calculated for each point and used in the TERMA calculations [7]. This is done by ray tracing and multiplying path length increments with corresponding average electron density [7].

To account for energy deposited about a primary interaction site a kernel, often created with MC calculations, is used. A point kernel is created by letting a photon interact at a point and then noting how much energy is emitted in each voxel, this energy is then divided by the total energy imparted [7]. This means that the kernel consists of the so-called fractional energy for each voxel [7].

When both the TERMA and kernels are obtained the dose distribution can be calculated using a convolution of the two [7],

$$D(r) = \int_{r'} T(r')H(r-r')d^3r. \tag{2.3}$$

TERMA $T(r')$ is the total energy imparted to a mass unit, $H(r-r')$ is the kernel value at the displacement from its origin. By integrating overall points, r', the total dose at point r is calculated. When in a homogeneous media $H(r-r')$ is not spatially dependent and the calculation can be done in the frequency space, where $D = T \otimes H$.

When calculating the dose distribution in a inhomogeneous region the kernel will also depend on r', making it no longer spatially invariant. A new scaled kernel is created used using the average electron density, ρ_{ave} between r and r'

$$H(r', r-r') = H(\rho_{\text{ave}}, r-r')\frac{\rho(r)}{\rho_{\text{ave}}}. \tag{2.4}$$

The TERMA and kernels described above are defined for monoenergetic sources. To account for the polyenergetic nature of most sources used within radiation treatment either a polyenergetic TERMA and kernels can be calculated or separate monoenergetic TERMA and kernels can be used, and the convolution calculations performed in a component-by-component way and then summed together.

2.2.3 Analytical Anisotropic Algorithm - AAA

The analytical anisotropic algorithm is a 3D pencil beam convolution-superposition algorithm developed by Varian and used in the TPS Eclipse [13]. It is a fast algorithm with the disadvantage of limitations in its accuracy.

Pencil beam algorithms are a variant of the convolution-superposition method discussed in section 2.2.2. These algorithms use pencil beam dose distributions, equivalent to a kernel but with per unit primary photon collision density instead of per unit energy imparted [7]. These pencil beam kernels are created from a point kernel by integrating along ray lines from the source [9]. Using pencil beam kernels decreases the computational power necessary to calculate the dose and increases the speed of the algorithm. Pencil beam kernel cannot take lateral scattering and scaling into account, which decreases its accuracy.

AAA can be seen as a refined version of the classic pencil beam algorithms as it does take lateral electron density and scattering its account. The A for ”analytical” comes from that a sum of exponential functions is used to approximate the lateral spread of the kernel [9]. This spread is then scaled separately for several discrete directions with the electron density, hence the A for ” anisotropic” [9]. MC is used to produce the monoenergetic pencil beam kernels used in AAA and polyenergetic scatter kernels are constructed by making a weighted summation of these kernels [13].

The AAA beam model is divided into three components primary photon fluence, extra focal photon fluence, and contamination electrons [13]. The initial phase-space of the

beam model and beam characteristics such as energy spectrum and intensity profile are produced by using MC simulations. These parameters are then modified to match measured data from each treatment unit [13]. The broad clinical beam is then also divided into finite-sized beamlets [13]. When calculating the dose distribution, the patient or phantom geometry is divided into divergent voxels aligning with the fanlines of these beamlets [13]. Separate convolutions for the three components of the beam model are done for each beamlets [13]. These convolutions are then combined using superposition to calculate the final dose [13].

In all calculations, AAA considers all mediums as water but takes their varying electron density into account. Because of this, AAA transports and calculates the dose as dose-to-water.

2.2.4 Collapsed Cone - CC

Collapsed cone algorithms use the superposition-convolution method described in section 2.2.2 with point kernels but do a collapsed cone approximation [7]. In the collapsed cone approximation, each interaction site is seen as the highest point of a set of lines with polar and azimuthal angles spreading out in 3 dimensions. These lines are considered the axles of cones. The energy deposited in this cone at radius r is collapsed into its line as the kernel functions along it. So, in an interaction point, the fractional energy is deposited along these collapsed lines, instead of in all voxels in the cones. The big advantage of this approximation is more accurate kernels compared to the pencil beams but still much faster than if point kernels would be used.

Both algorithms from DC and RS are collapsed cone algorithms and function generally in the same way. Both implementations of CC use inverse ray tracing when calculating the TERMA and kernels. Inverse ray tracing rays are cast from each TERMA voxel back to the fluence plan and the cone is collapsed inward. Inverse ray tracing enables paralleling of the algorithm and the use of GPU. GPU stands for graphics processing unit and has a parallel structure, making parallel calculating possible which enables faster calculations.

A difference between RS and DC is that RS only uses effective density to correct for inhomogeneities [14], thus calculating dose-to-water. The effective density RS utilizes is calculated based on mass density obtained from the CT images, but corrected for the increase of par production present at higher energies, >10 MV [14]. DC also corrects for energy absorption coefficients for different materials [9][15]. Water is one of the materials DC uses, which means that in soft tissue the dose can be regarded as dose-to-water [9]. When it comes to other materials such as bone and lung tissue DC can be seen as leaning more towards presenting the dose as dose-to-medium.

2.2.5 Acuros XB - AXB

Acuros XB is a so-called grid-based Boltzmann solver developed by Varian and used in the TPS Eclipse. It is based on numerically solving the linear Boltzmann transport

equation and was developed to be both fast and have great accuracy as it takes heterogeneities directly into account [16].

The possible achievable accuracy of AXB and MC simulations is equivalent and only limited by uncertainties in the particle interaction data and the problem being analyzed [16]. The errors in these algorithms are however fundamentally different. In MC, the errors are random and result from simulating a finite number of particles while the errors in AXB are systematic and arise from the discretization of variables in space, angle, and energy [16]. The lack of statistical error in AXB is a reason for its development, along with the possible high-speed [16].

AXB uses the same multiple source model as AAA, see section 2.2.3, and the calculations are performed in four steps [16]. Step one consists of the transport of the source model fluence into the patient or phantom geometry. In steps two and three the scattered photon and electron fluence is calculated, this includes an angle and energy discretization and the linear Boltzmann equation is solved iteratively. The dose in any voxel is determined in step four by using an energy-dependent fluence-to-dose response function.

While convolution-superposition algorithms handle heterogeneities by corrections applied to the dose kernels, AXB explicitly models the physical interactions in the mediums [16]. AXB can calculate the dose as both dose-to-water and dose-to-medium. When dose-to-water the energy-dependent response function is based on water with varying densities [16].

When calculating dose-to-medium AXB requires the chemical compositions of the mediums, which is done by providing the mass density and material type in each voxel based on the CT images [16]. AXB includes five pre-defined tissue types: lung, adipose tissue, skeletal muscle, cartilage, and bone as well as 16 non-biologic materials including air and water [16].

3

Validation of Monte Carlo 6FFF Accelerator Model in Water Phantom

The main aim of the first part of this thesis was to validate the MC 6FFF accelerator model against measured data. This part also included a calculation of a calibration factor to convert the MC distribution to absolute dose, Gy, as well as a water phantom MC evaluation of the algorithms AAA, AXB, DC, and RS. This chapter will present the methods used, the following results as well as a corresponding discussion.

3.1 Method

The MC calculations were performed by the EGSnrc code system and the accelerator head was modeled in the code system BEAMnrc. Jaws and multi-leaf collimators used to shape the radiation field have been validated earlier. A pre-calculated generation 2 phase space above jaws, provided by Varian, was used as input to produce phase spaces below jaws with field sizes 4x4 cm^2, 10x10 cm^2, and 20x20 cm^2. These were further used to calculate dose distributions in the water phantom (code DOSXYZnrc). The settings used when producing these phase spaces are presented in table 3.1, and no variance reduction method was used. The phase spaces were built by generating multiple phase spaces, with different seeds, and then combining them using the program BEAMdp. The size of each phase space was adjusted so that all field sizes gave approximately $37 \cdot 10^6$ photons per cm^3.

To generate dose distributions in water phantoms the MC simulation system DOSXYZnrc was used with the BEAMnrc produced phase spaces as input. The simulation settings used for DOSXYZnrc are presented in the table 3.1, and no variance reduction was used. The number of histories used was adjusted so that the statistical error in the calculations was around 1%. The SSD in the MC calculations was adapted to the SSD used during the corresponding measurement.

Table 3.1: The settings of most importance used in the MC simulations when BEAMnrc respectively DOSXYZnrc was used.

	BEAMnrc	**DOSXYZnrc**
ECUT [MeV]	0.7	0.7
PCUT [MeV]	0.01	0.01
Max step size [cm]	5	5
Photon BCA	PRESTA-I	EXACT
Electron BCA	PRESTA-II	PRESTA-II

The MC calculations were compared to measured data using PDD curves, output factors, and profiles at the depths of 14 mm, 50 mm, and 100 mm. As the unit for the measured data used was in relative dose [%], the measured data and MC calculations were normalized prior to the comparison. The 10x10 cm^2 depth dose curve was normalized to 100 % at depth 100 mm, using interpolation of 9 points. The depth dose curves for field sizes 4x4 cm^2 and 20x20 cm^2 were then normalized at 100 mm depth with calculated output factors. All profiles were normalized at the center according to the corresponding depth dose curve, already normalized. The difference in the PDD curve was calculated using equation (3.1) and the difference between the profiles using equation (3.2), were D_{MC} and D_{meas} refers to the MC calculated and measured dose.

$$d_{PDD} = (D_{MC} - D_{meas})/D_{MC} \tag{3.1}$$

$$d_{profile} = D_{MC} - D_{meas} \tag{3.2}$$

The water phantom used in the MC calculations was defined using DOSXYZnrc. Voxel sizes were chosen to be as close as possible to the size of the ionizing chamber (IC) used for the measured data but also so that the central line, as well as the profiles, would run in the center of voxels. What voxel sizes and ionizing chamber dimensions were used is presented in table 3.2.

Table 3.2: Voxel sizes used in the MC calculations and the dimensions of the ionizing chamber used for the measurements, presented for each field size.

Field size cm^2	Ionization chamber [cm^3]	MC voxel size [cm^3]
4x4	0.4x0.4x0.38	0.4x0.4x0.4
10x10	0.4x0.4x0.38	0.4x0.4x0.4
20x20	0.6x0.6x0.58	0.6x0.6x0.4

A conversion factor, to convert the MC dose with unit Gy per incident particle to Gy/MU, was determined using the above-mentioned MC calculations. The calibration factor was used to calibrate the MC system used in part two of the thesis, but also to compare the MC calculated distributions in water with AAA, AXB, DC, and RS in absolute dose [Gy]. The conversion factor, K_{MC}, was determined using a method presented by Richard Ottosson in his Ph.D. thesis [2].

$$K_{MC} = \frac{D_{ref}^{meas}}{D_{ref}^{MC}}, \tag{3.3}$$

where $D_{\text{ref}}^{\text{meas}}$ and $D_{\text{ref}}^{\text{MC}}$ are the dose in a reference point measured respectively calculated with MC. The reference point used in this thesis was the dose at 10 cm depth along the central axis with SSD=90 cm and field size 10x10 cm^2. The absolute dose in Gy can then be determined using the equation

$$D_{\text{MC,abs}} = D_{\text{MC}} \cdot K_{\text{MC}} \cdot U, \tag{3.4}$$

where D_{MC} is the dose given by the MC method and U is the MU used, divided by the number of MU used when calculating K_{MC}, which was 120 MU in the reference point.

To calibrate the MC system a conversion factor was first determined and then evaluated by calculating the dose in the reference point in a water phantom. The factor was then adjusted so that the MC system produced the dose $D_{\text{ref}}^{\text{MC}} = 1$ Gy in the reference point.

Lastly, the algorithms AAA, AXB, DC, and RS were compared with MC calculations in reference conditions and absolute dose. PDD curves and profiles at depths 14 mm, 50 mm, and 100 mm were used in this comparison. All of these calculations were done with voxel size 0.25x0.25x0.25 cm^3. Both dose-to-medium and dose-to-water dose distributions were calculated with AXB, AXB_{w}, and AXB_{m}. The reason for this is that the water phantom was created using CT images, and the interpretation may vary.

3.2 Results

The MC calculated distributions were evaluated both by comparing depth dose curves and profiles with the measured data. Figures 3.1, 3.2 and 3.3 shows the results of the depth dose curve evaluation for the different field sizes. The curves are normalized as described in section 3.1. The difference between the MC calculations and the measured data varies between around -2% and 1.5%, but generally within -1% to 1%. The mean and max of the total statistical error in the MC calculations calculated as a percentage of the dose are presented in table 3.3.

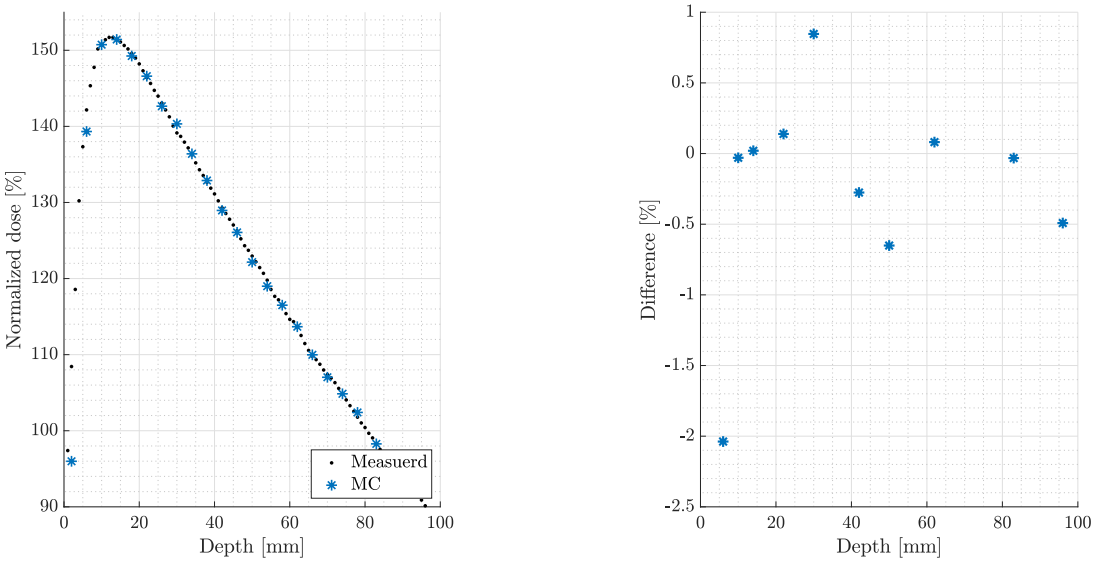

Figure 3.1: Left figure showing the measured and MC calculated depth dose curve in water phantoms, with field size 4x4 cm^2. Normalized dose [%] on the y-axis and depth in the water phantoms on the x-axis. The calculation of the normalized dose is described in section 3.1. The right figure shows the difference, as a percentage of the MC dose.

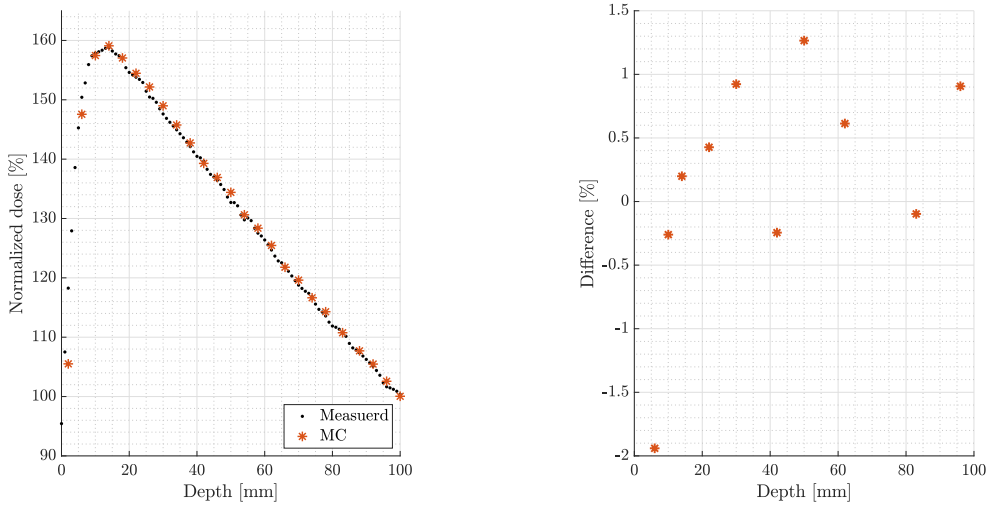

Figure 3.2: Left figure showing the measured and MC calculated depth dose curve in water phantoms, with field size 10x10 cm^2. Normalized dose [%] on the y-axis and depth in the water phantoms on the x-axis. The calculation of the normalized dose is described in section 3.1. The right figure shows the difference, as a percentage of the MC dose.

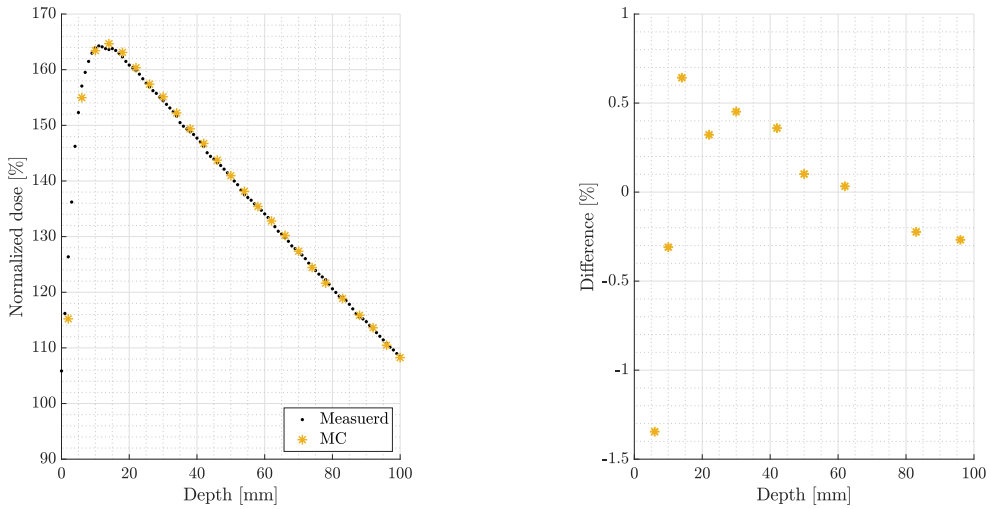

Figure 3.3: Left figure showing the measured and MC calculated depth dose curve in water phantoms, with field size 20x20 cm^2. Normalized dose [%] on the y-axis and depth in the water phantoms on the x-axis. The calculation of the normalized dose is described in section 3.1. The right figure shows the difference, as a percentage of the MC dose.

Table 3.3: The mean and max of the total statistical error calculated as a percentage of the dose along the depth axis for respective field size.

Field size cm^2	Mean error [%]	Max error [%]
4x4	0.92	1.27
10x10	0.72	0.95
20x20	0.47	0.62

Figures 3.4, 3.5 and 3.6 presents the measured and MC calculated profiles for the three field sizes at depths 14 mm, 50 mm and 100 mm respectively. All profiles are normalized according to the description in section 3.1. The difference between measured data and MC calculations was calculated by interpolating the MC calculations to the positions in the measured data. The main differences were found as the normalized dose increased from around 2% to 80%, henceforth referred to as the extended penumbra. Mainly in the area were the dose increased from 5-15%. This difference can be caused by differences in the voxel discretization, or spatial differences. The spatial differences in the extended penumbra were found to vary between 0 mm and 2 mm. The difference in the center of the profiles was found to be < 1%, for all field sizes and depths excluding 20x20 cm^2 at depth 14 mm and 10x10 cm^2 at depth 50 mm where a bigger difference can be seen.

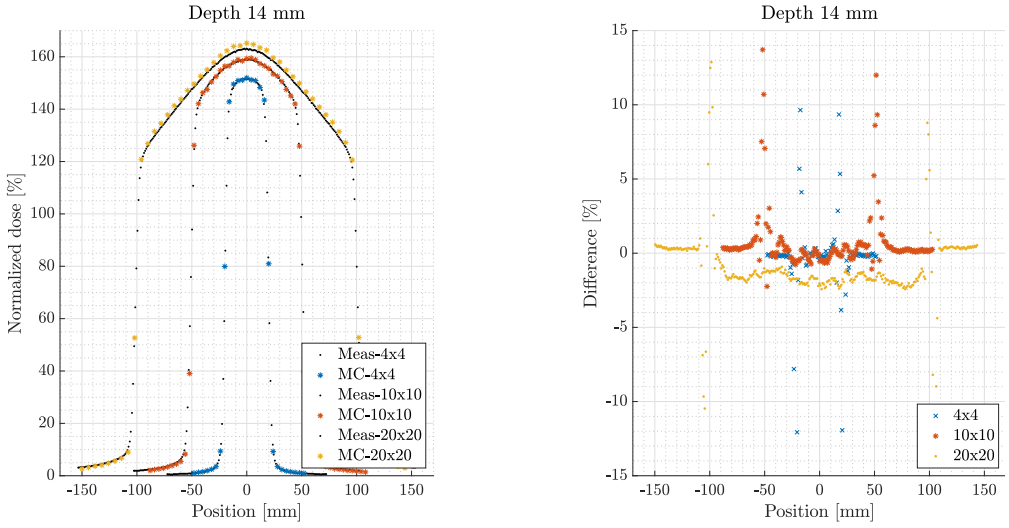

Figure 3.4: In left figure measured and MC calculated profiles for three field sizes is shown. Normalized dose on the y-axis and position along the profile on the x-axis, where the normalized dose is calculated as described in section 3.1. The difference between the measured and MC calculated profiles are presented in the right figure.

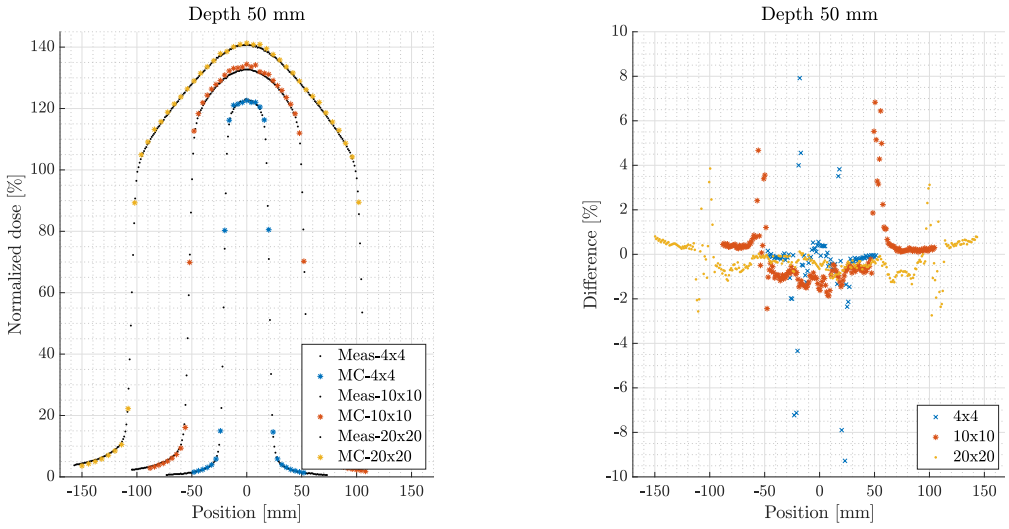

Figure 3.5: In left figure measured and MC calculated profiles for three field sizes is shown. Normalized dose on the y-axis and position along the profile on the x-axis, where the normalized dose is calculated as described in section 3.1. The difference between the measured and MC calculated profiles are presented in the right figure.

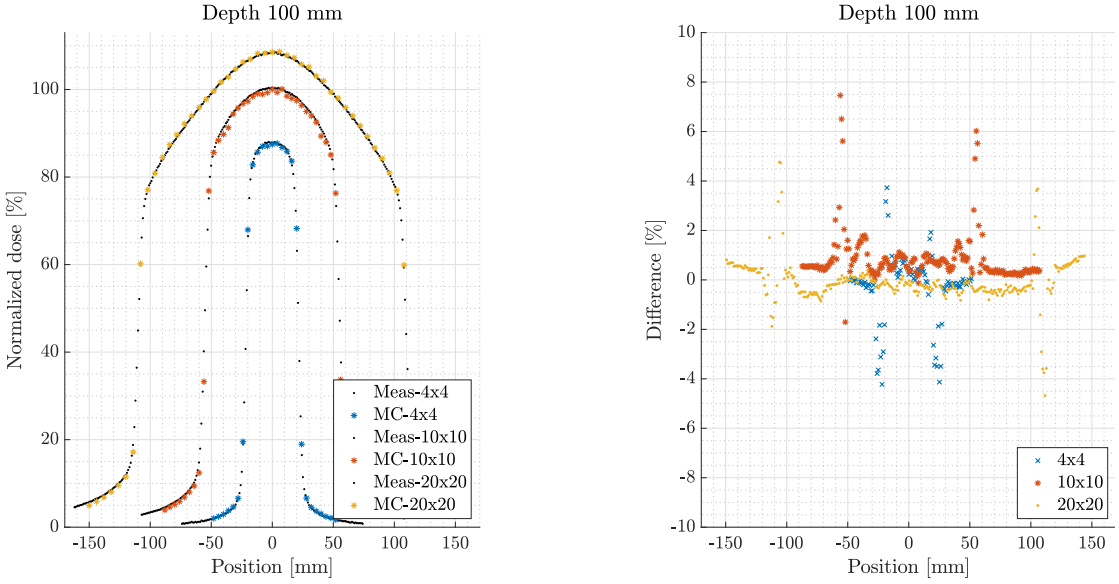

Figure 3.6: In left figure measured and MC calculated profiles for three field sizes is shown. Normalized dose on the y-axis and position along the profile on the x-axis, where the normalized dose is calculated as described in section 3.1. The difference between the measured and MC calculated profiles are presented in the right figure.

In table 3.4 measured and MC calculated output factors, OF, are presented as well as the difference between them. The difference is calculated as the percent of the MC calculated OF.

Table 3.4: Measured OF and MC calculated OF presented for field sizes 4x4 cm^2 and 20x20 cm^2. The difference between measured and MC-calculated OF is calculated as the percent of the MC calculated OF.

Field size [cm^2]	Measured OF	MC calculated OF	Difference [%]
4x4	0.877	0.874	0.30
10x10	1	1	1
20x20	1.085	1.085	0.00

3.2.1 Calculation of Calibration Factor

When interpolating the data, the $D_{\text{ref}}^{\text{MC}}$ was determined to $2.3258 \cdot 10^{16}$ Gy/iP, which gave $K_{\text{MC}} \approx 358 \cdot 10^{11}$. This calibration factor was tested with the MC system and then modified to

$$K_{\text{MC}} = 35'919'540'229'885.1$$

which gave $D_{\text{MC}} = 1$ Gy at depth 100 mm.

3.2.2 Evaluation of Algorithms Against MC in Water Phantom

Figures 3.7 and 3.8 show the result of the 6FFF depth dose curve evaluation of AAA, AXB_m, AXB_w, RS and DC against MC-method, absolute dose comparison. The difference in the depth dose curves from the MC data was calculated by interpolating all algorithms to the positions of the MC data. The biggest differences were found before dose max, excluding these points, the difference was found to vary between -0.05 Gy to 0.02 Gy. Generally, the biggest difference from MC is DC.

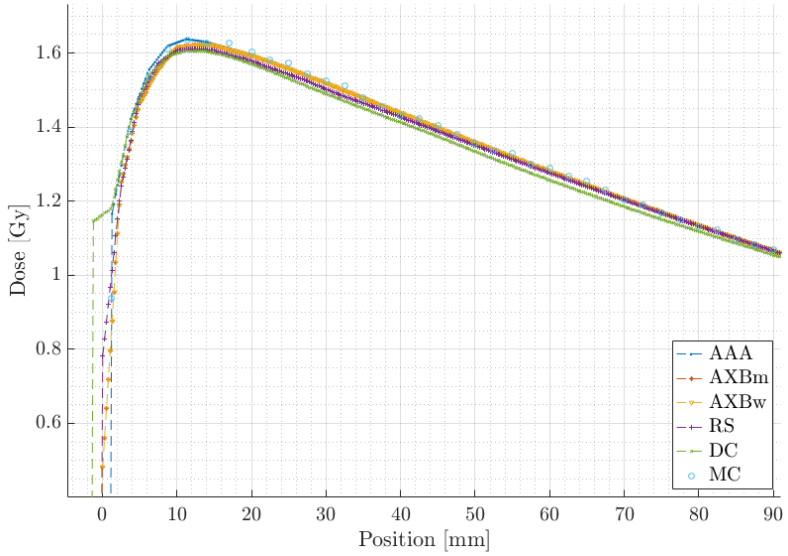

Figure 3.7: Depth dose curves for 6FFF dose distributions calculated with the five algorithms AAA, AXB_m, AXB_w, RS and DC in a water phantom.

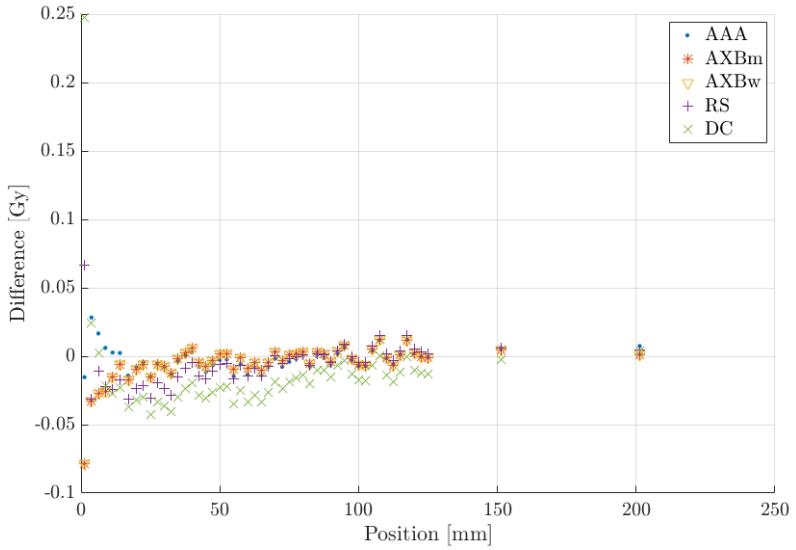

Figure 3.8: The difference in Gy between the MC calculations and the four algorithms (AAA, AXB_m, AXB_w, RS and DC), plotted against the position along the depth axis.

An evaluation of the profiles at depths 14 mm, 50 mm, and 100 mm of the algorithms

AAA, AXB_m, AXB_w, RS, and DC against MC calculated data is shown in figures 3.9 to 3.12. Figures 3.10, 3.11 and 3.12 profiles at depths 14 mm, 50 mm and 100 mm. The differences between the mentioned algorithms and the MC calculated data in the center of the profiles (penumbra excluded) are presented in figure 3.9.

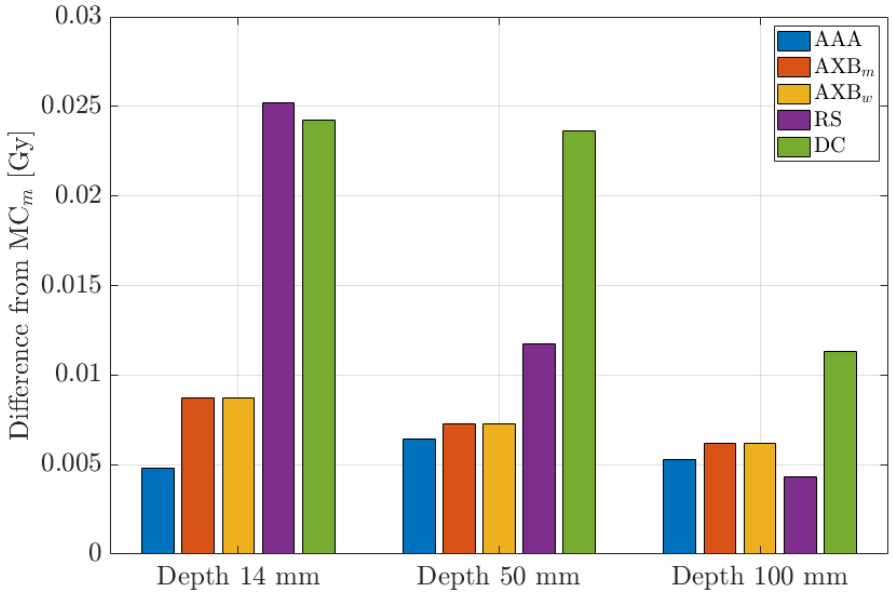

Figure 3.9: A bar plot showing the mean difference in Gy between the MC calculations and the four algorithms (AAA, AXB, RS, and DC) at the center of the water phantom profiles.

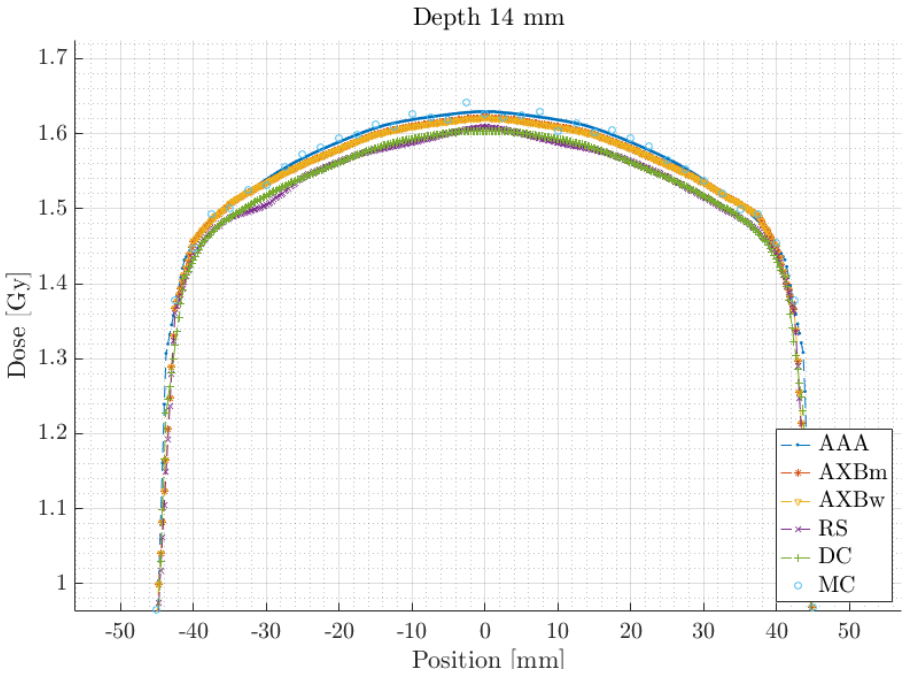

Figure 3.10: Profiles at depth 14 mm calculated in a water phantom for the five algorithms (AAA, AXB, RS, DC, and MC) in absolute dose [Gy]. Zoomed in at the center of the profiles to show the difference between the algorithms more clearly.

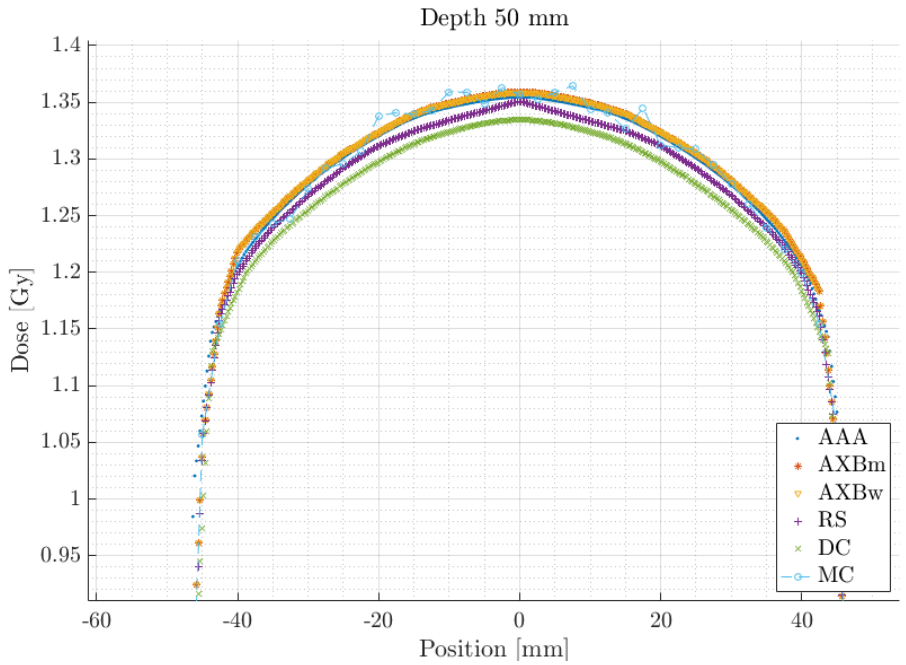

Figure 3.11: Profiles at depth 50 mm calculated in a water phantom for the five algorithms (AAA, AXB, RS, DC, and MC) in absolute dose [Gy]. Zoomed in at the center of the profiles to show the difference between the algorithms more clearly.

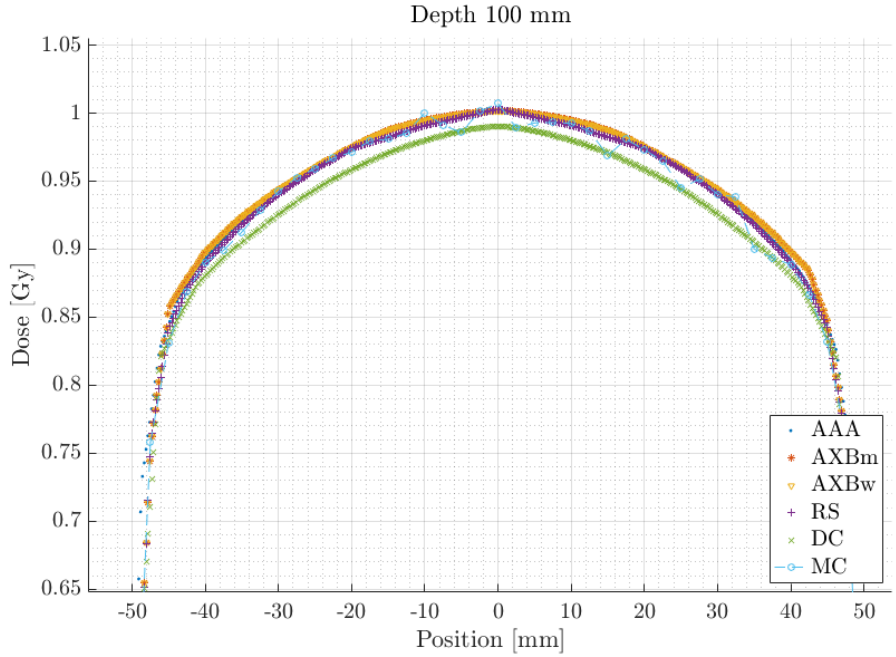

Figure 3.12: Profiles at depth 100 mm calculated in a water phantom for the five algorithms (AAA, AXB, RS, DC, and MC) in absolute dose [Gy]. Zoomed in at the center of the profiles to show the difference between the algorithms more clearly.

3.3 Discussion

The results show that the MC dose distributions calculated in a water phantom generally had a dose difference of < 2% from measured data, except for in the extended penumbra of the profiles. These larger differences in the extended penumbra are believed to be derived from differences in the discretization causing small spatial differences that have a larger impact on steep dose gradients. The spatial differences in this area were estimated to be up to 2 mm. In the center of the profiles the differences were between -1 % and 1 % for most depths and field sizes, larger differences were found in at depth 14 mm for 20x20 cm^2. This larger difference is believed to come from the normalization done from the depth dose curve, see figure 3.3. Overall, the differences found is considered comparable to the statistic error of the MC calculations, see table 3.3. Based on these results and the negligible difference in the OF the 6FFF MC model was considered validated.

To further evaluate the accuracy of the MC model more field sizes and depths could be examined. A more accurate evaluation would also be achieved if the absolute dose was compared instead of the normalized dose. A larger number of histories would also reduce the statistical error in the MC calculations. For the aim of this thesis, the evaluations made are considered sufficient, as the calibration coefficient was validated in the MC system.

When comparing the algorithms AAA, AXB, RS, and DC to MC the algorithm with the most similar profiles was AAA. This is somewhat unexpected as AXB is the algorithm with the most algorithmic similarities to MC. The algorithm with the biggest difference from MC is DC, as DC consistently underestimates the dose. A comparison between AAA and DC with energy 6 MV was also made, see figure A.1 in appendix A.1 and the same differences were not seen. This indicates that something in the DC beam model for FFF makes the dose underestimated. To further expand the MC evaluation AAA, AXB, RS, and DC more field sizes and depths could be explored and gamma evaluations could be used.

4

Evaluation of Flattening Filter Free Clinical Dose distributions

The second part of the thesis consisted of using the calibrated MC system to evaluate 6FFF dose distributions calculated in a heterogeneous lung phantom and various patient plans. This chapter will present the methods used to produce and evaluate these dose distributions along with the following results and discussion.

4.1 Method

The patient plans used in this thesis were all previously created for clinical use in the TPS Eclipse (clinical mode). To be used in this thesis the plans were exported to Eclipse research mode and in the process anonymized. For the plans to pass through the MC system, some modifications were made: the table was removed and if the treatment technique was SRS Arc Therapy it was changed to Arc Therapy. The removal of SRS was done as it was discovered that the SRS label made the MC system calculate the dose in the wrong area. In Eclipse Research mode the plan was calculated with AAA and then exported to the MC system to be recalculated.

When using the MC system the plans were first put through a test calculation using fewer histories. If the plans successfully passed the test a real calculation was started with 999'000'000 histories. For each plan, the MC system calculated both a dose distribution with dose-to-water referred to as MC_w and dose-to-medium, MC_m. These dose distributions were then imported to Eclipse.

Additional dose distributions were then calculated using $AXB_{m/w}$ (dose-to-water and dose-to-medium). The AAA calculated plan was exported to RS and DC and recalculated with their respective CC algorithm and then imported back to Eclipse.

The evaluation of the plans was done in Eclipse using dose volume histograms (DVH). The DVH parameters used in the evaluations were chosen based on target and risk organs dose-volume objectives and constraints, as well as what parameters were used in the study "Monte Carlo patient-specific pre-treatment QA system for volumetric modulated arc therapy" [17] so that the results easier could be compared. Altogether a total of 9 plans were evaluated, divided into four groups: phantom plan, prostate plans,

brain plans, and plans in the thorax region. Table 4.1 lists all the names of all plans evaluated, the resolution used, the treatment technique used, and the parameters used in the DVH evaluation.

Table 4.1: Overview of the plans evaluated against MC calculations, their treatment technique, resolution, and parameters evaluated.

Plan name	**Technique**	**Res.** [cm]	**Parameters**
Phantom	Static	0.25	D_{mean}(IC-lung), D_{mean}(IC-middle), D_{mean}(IC-vein), D_{mean}(lung), D_{mean}(SC), D_{mean}(IC-p)
Prostate1	Arc Therapy	0.25	D_{mean}(PTV), D_{mean}(CTV), $D_{98\%}$(PTV), $D_{2\%}$(PTV),$V_{90\%}$(rectum),$V_{50\%}$(rectum)
Prostate2	Arc Therapy	0.2	D_{mean}(PTV), D_{mean}(CTV), $D_{98\%}$(PTV), $D_{2\%}$(PTV),$V_{90\%}$(rectum),$V_{50\%}$(rectum)
Brain1	Arc Therapy	0.25	$D_{98\%}$(PTV), $D_{2\%}$(CTV), $D_{1\%}$(chiasm), $D_{0.1\%}$(brainstem), $D_{40\%}$(hippo.),D_{mean}(PTV)
Brain2	Arc Therapy	0.25	$D_{98\%}$(PTV), $D_{2\%}$(CTV), $D_{1\%}$(chiasm), $D_{0.1\%}$(brainstem) ,$D_{40\%}$ (hippo.),D_{mean}(PTV)
Thorax1(SBRT)	Arc Therapy	0.2	D_{min}(GTV), D_{mean}(GTV), D_{mean}(PTV), D_{mean}(lung),$D_{2\%}$(SC),$D_{98\%}$(PTV)
Thorax2(SBRT)	Static	0.15	D_{min}(GTV), D_{mean}(GTV), D_{mean}(PTV), D_{mean}(lung),$D_{2\%}$(SC),$D_{98\%}$(PTV)
Thorax3(Lung)	Arc Therapy	0.2	D_{min}(GTV), D_{mean}(GTV), D_{mean}(PTV), D_{mean}(lung),$D_{2\%}$(SC),$D_{98\%}$(PTV)
Thorax4(Esophagus)	Arc Therapy	0.25	D_{min}(GTV), D_{mean}(GTV), D_{mean}(PTV), D_{mean}(lung),$D_{2\%}$(SC),$D_{98\%}$(PTV)

A CT image of the lung phantom used can be seen in figure 4.1 together with the structures used in the evaluation. The field size used in the phantom plan was 20x20 cm^2 with an isocenter at [7,0,0] cm and 120 MU.

As DC is currently used as a QA dose distributions calculated with DC were also directly compared to algorithms AAA and $AXB_{m/w}$. The comparison was done by calculating the differences in the DVH parameters as well as noting the gamma pass rate given when DC recalculated the AAA dose distribution.

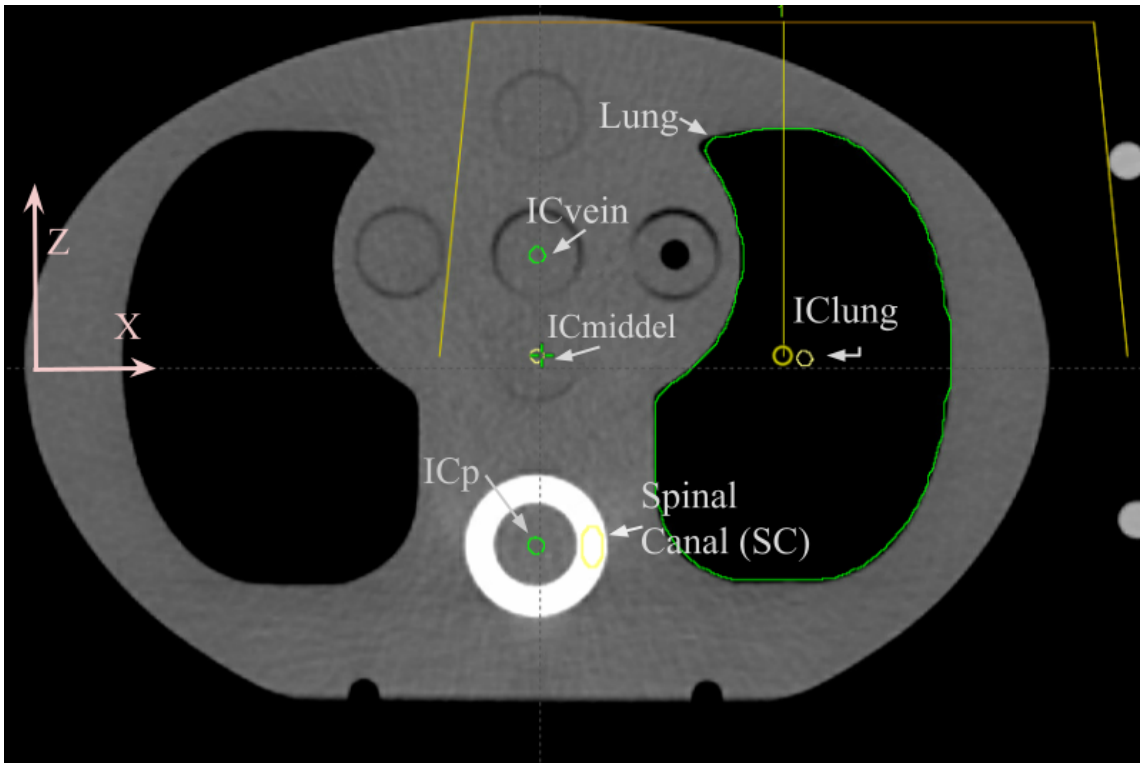

Figure 4.1: An CT image of the lung phantom used in the study with the DVH structures pointed out. The yellow lines in the upper part of the figure indicate where the field was applied.

4.2 Results

In the following sections, the results of the MC evaluation of 9 plans will be presented. All doses and differences are presented in relative dose with unit %, that is the percentage of the total treatment dose in each plan. In sections 4.2.1 to 4.2.4 the results of each plan evaluation are reported, and in section 4.2.5 an overview of all results is presented.

For each plan algorithm, AAA, AXB_m and RSs CC-algorithm are compared to MC_w and AXB_m to MC_m. DCs CC-algorithm is compared both to MC_w and MC_m.

4.2.1 Lung Phantom

The results of the phantom evaluation are presented in figure 4.2, where the difference in the DVH parameters in relative dose is shown for each algorithm. The difference varies from 2.4% and -2%. The DVH parameter with the overall biggest differences is D_{mean}(ICp) where all algorithms have a difference > 1%. Algorithms AAA and DC stand out with big differences in the parameter D_{mean}(IClung), whereas the other algorithms have either a difference < 0.5% or a negative difference ≤ -1.5%.

The biggest difference between the evaluated algorithms and MC was found inside of bone equivalent materials, D_{mean}(ICp), and for algorithms AAA and DC also around lung equivalent material, D_{mean}. The mean difference over all parameters is < 2% for all algorithms and <1% for AXB_m. Only algorithms AAA and RS exceed 2% difference, in one parameter each.

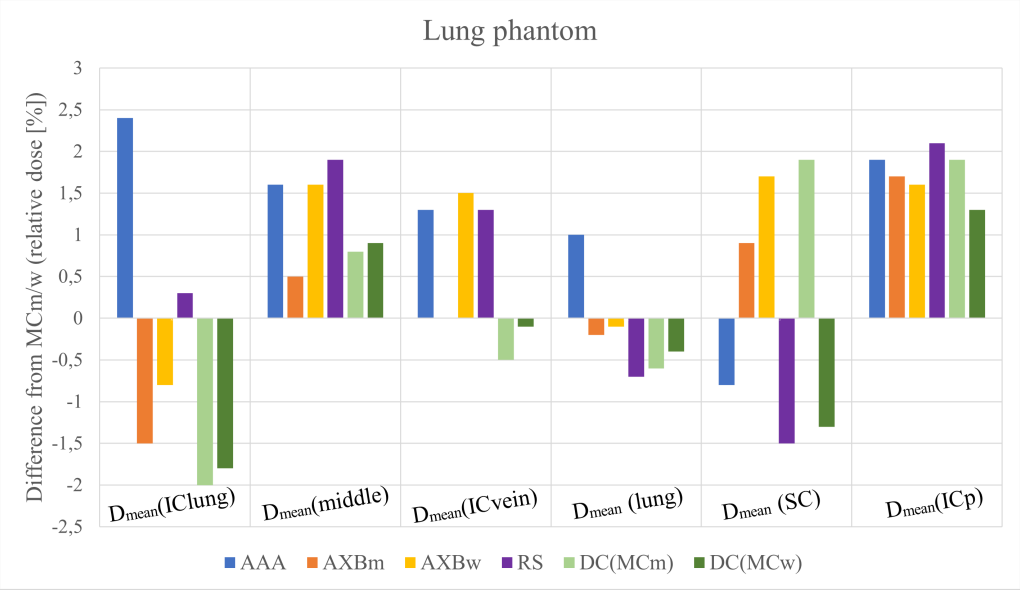

Figure 4.2: A bar plot over the differences between the algorithms AAA, $AXB_{m/w}$, RS, and DC from the MC calculated distribution. Algorithms AAA, AXB_w and RS are compared to MC_w, AXB_m is compared to MC_m and DC is compared to MC_m and MC_w. The differences are calculated in relative dose by subtracting the value of the $MC_{w/m}$ from the value of the respective algorithm.

4.2.2 Prostate Plans

The results of the evaluation of plans Prostate1 and Prostate2 are shown in figures 4.3 and 4.4 respectively. For Prostate1 the biggest differences are found in parameter $D_{2\%}$(PTV) where both algorithms RS and DC differ more the 2%. It should be noted that there were 3 gold markers in PTV for Prostate1, which caused some artifacts in the CT images. Mainly RS but also DC stands out with bigger differences in the target parameters than the remaining algorithms.

Algorithms AAA and $AXB_{w/m}$ do not exceed a difference of 2% in any of the parameters in Prostate1 and have a mean difference over all parameters under 1%. Both RS and DC exceed a 2% difference, RS on multiple occasions.

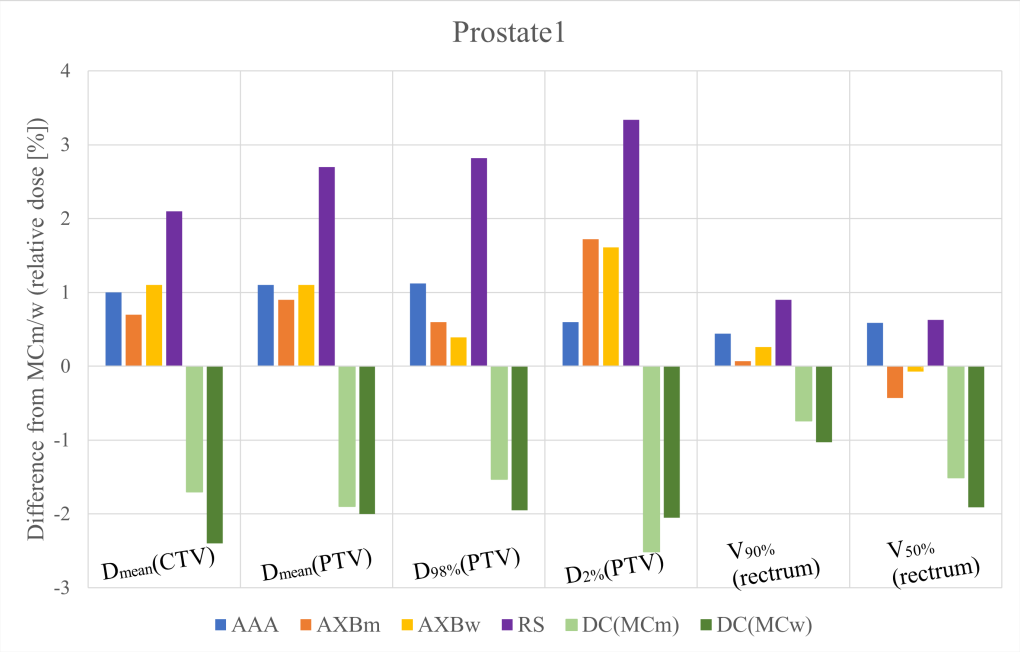

Figure 4.3: A bar plot over the differences between the algorithms AAA, $AXB_{m/w}$, RS, and DC from the MC calculated distribution. Algorithms AAA, AXB_w and RS are compared to MC_w, AXB_m is compared to MC_m and DC is compared to MC_m and MC_w. The differences are calculated in relative dose by subtracting the value of the $MC_{w/m}$ from the value of the respective algorithm.

In the evaluation of Prostate2, see figure 4.4, the big differences are found in parameter $D_{98\%}$(PTV) where all algorithms except DC exceed a difference of 2%. Oppose to Prostate1 rather small differences are instead seen in parameter $D_{2\%}$(PTV). Potentially this could be caused by the patient's geometry, as parts of bone were close to and inside of PTV.

Except for parameter $D_{98\%}$(PTV) the differences are < 2%, for all algorithms when DC is compared to MC_m, but generally closer to 1% then 2%, in many places < 1%.

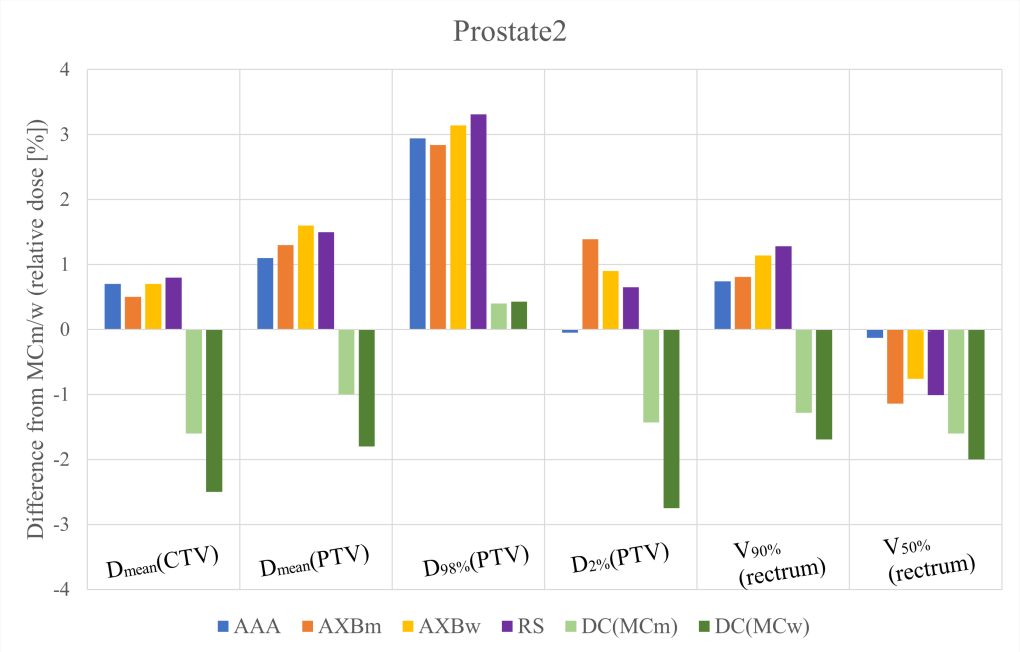

Figure 4.4: A bar plot over the differences between the algorithms AAA, $AXB_{m/w}$, RS, and DC from the MC calculated distribution. Algorithms AAA, AXB_w and RS are compared to MC_w, AXB_m is compared to MC_m and DC is compared to MC_m and MC_w. The differences are calculated in relative dose by subtracting the value of the $MC_{w/m}$ from the value of the respective algorithm.

4.2.3 Brain Plans

Figures 4.5 and 4.6 present the MC evaluations of plans Brain1 and Brain2. In both plans the differences for AAA and $AXB_{m/w}$ less the 2% in all cases and in most cases less the 1.5%. Parameters $D_{0.1\%}$(Brain stem) and $D_{40\%}$(Hippocampus) have in plan Brain1 the biggest difference but in plan Brain2 the smallest. A probable reason for this is the difference in treatment location and patient geometry. In plan Brain1 the brain stem and hippocampus are very close to and in some places in the PTV, which makes the structures subject to big dose gradients. Brain2 instead has a larger distance between these OAR and the PTV resulting in less dose to the OAR and only small dose gradients.

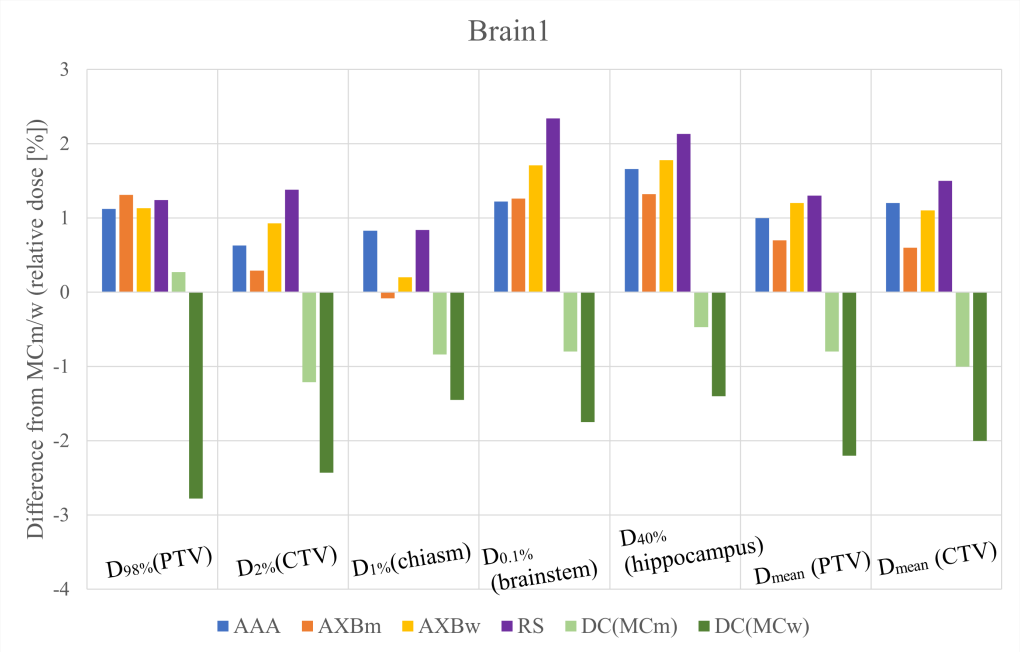

Figure 4.5: A bar plot over the differences between the algorithms AAA, $AXB_{m/w}$, RS, and DC from the MC calculated distribution. Algorithms AAA, AXB_w and RS are compared to MC_w, AXB_m is compared to MC_m and DC is compared to MC_m and MC_w. The differences are calculated in relative dose by subtracting the value of the $MC_{w/m}$ from the value of the respective algorithm.

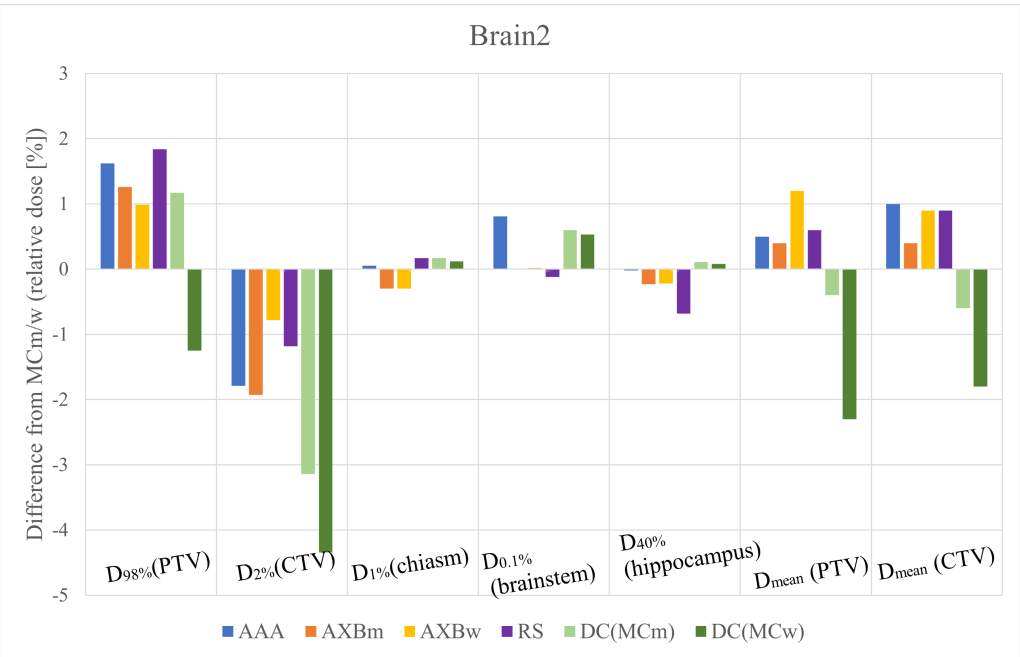

Figure 4.6: A bar plot over the differences between the algorithms AAA, $AXB_{m/w}$, RS, and DC from the MC calculated distribution. Algorithms AAA, AXB_w and RS are compared to MC_w, AXB_m is compared to MC_m and DC is compared to MC_m and MC_w. The differences are calculated in relative dose by subtracting the value of the $MC_{w/m}$ from the value of the respective algorithm.

4.2.4 Plans in the Thorax Region

The results of the MC evaluations in the thorax region are presented in figures 4.7, 4.8, 4.9 and 4.10. In plan Thorax1(SBRT) algorithm DC stands out with big negative differences, in most cases exceeding a -2% difference, this compared to AAA and $AXB_{m/w}$ that has differences ≤ 2.1%. In plan Thorax2(SBRT) both algorithms AAA and DC stand out with differences > 4% in parameter $D_{98\%}$(PTV) and $D_{2\%}$(CTV) respectively. The risk organ-related parameters D_{mean}(Lung) and $D_{2\%}$(SC) have overall algorithms small differences, < 0.7%. A reason for the small differences can be that the risk organs in these plans receive only small doses, a relative dose < 25%.

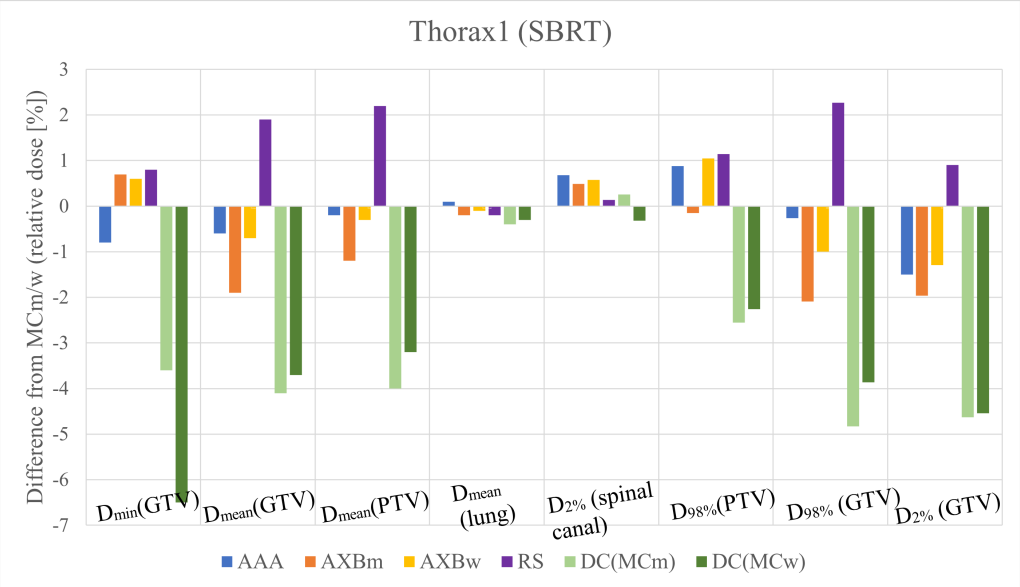

Figure 4.7: A bar plot over the differences between the algorithms AAA, $AXB_{m/w}$, RS, and DC from the MC calculated distribution. Algorithms AAA, AXB_w and RS are compared to MC_w, AXB_m is compared to MC_m and DC is compared to MC_m and MC_w. The differences are calculated in relative dose by subtracting the value of the $MC_{w/m}$ from the value of the respective algorithm.

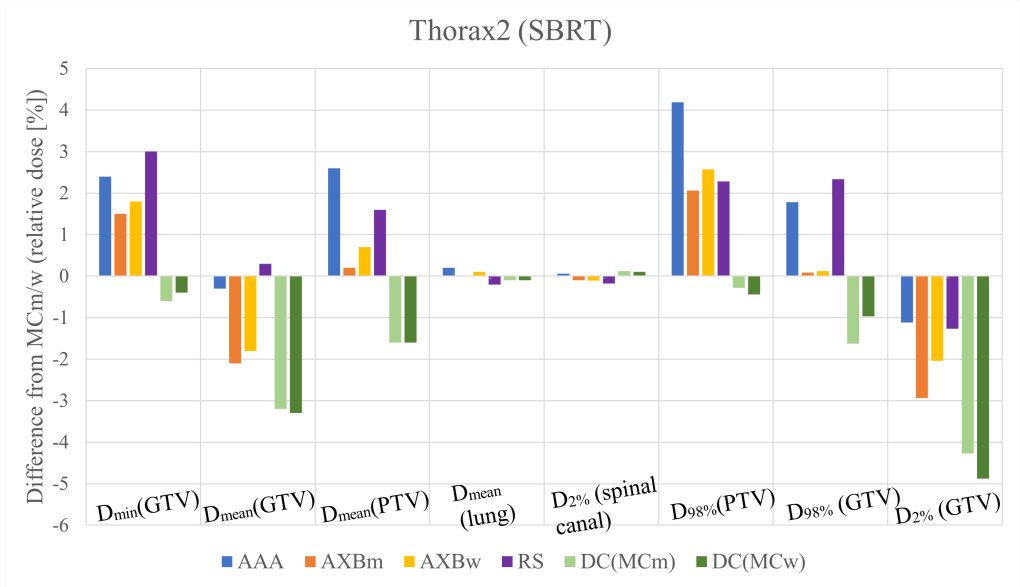

Figure 4.8: A bar plot over the differences between the algorithms AAA, $AXB_{m/w}$, RS, and DC from the MC calculated distribution. Algorithms AAA, AXB_w and RS are compared to MC_w, AXB_m is compared to MC_m and DC is compared to MC_m and MC_w. The differences are calculated in relative dose by subtracting the value of the $MC_{w/m}$ from the value of the respective algorithm.

The evaluation of plan Thorax3(lung) is presented in figure 4.9. Compared to plans Thorax1 and Thorax2, for Thorax3 bigger differences are seen in the target parameters, as DC on multiple occasions exceeds a difference of 6%. Algorithms AAA, $AXB_{m/w}$, and RS also exceed a difference of 2% in most target parameters. The risk organ-related parameters have only very small differences, as well as overall small doses, with relative dose < 11%. In the evaluation of plan Thorax4(esophagus) algorithms DC is closer to MC compared to plan Thorax3, and all algorithms have differences ≤ 3.5%. Bigger differences in the risk organ-related organs can be found in plan Thorax4 compared to the other thorax plans. For $D_{2\%}$(SC) this can be caused by a bigger dose, the relative dose was around 50%.

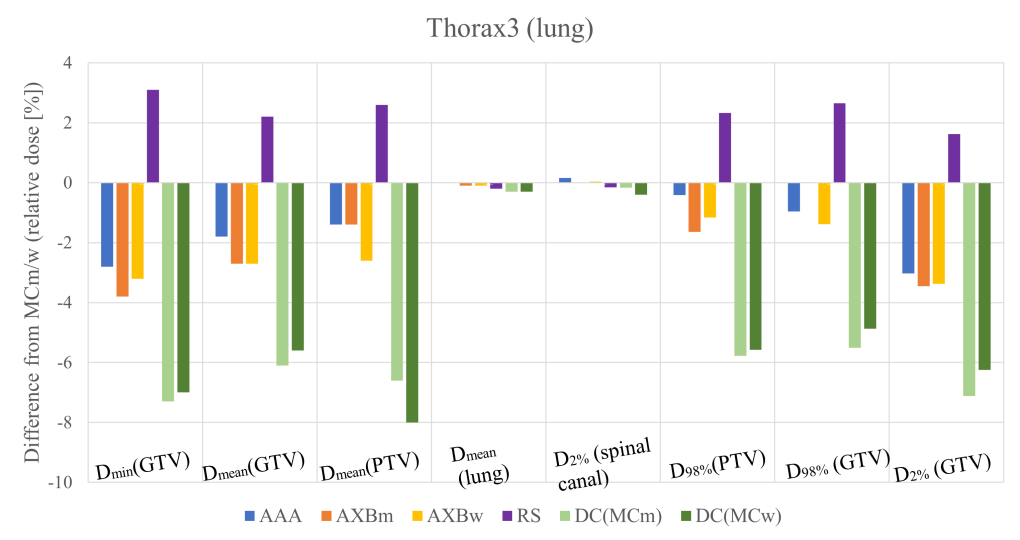

Figure 4.9: A bar plot over the differences between the algorithms AAA, $AXB_{m/w}$, RS, and DC from the MC calculated distribution in plan Lung1. Algorithms AAA, AXB_w, and RS are compared to MC_w and AXB_m and DC is compared to MC_m. The differences are calculated in relative dose by subtracting the value of the $MC_{w/m}$ from the value of the respective algorithm.

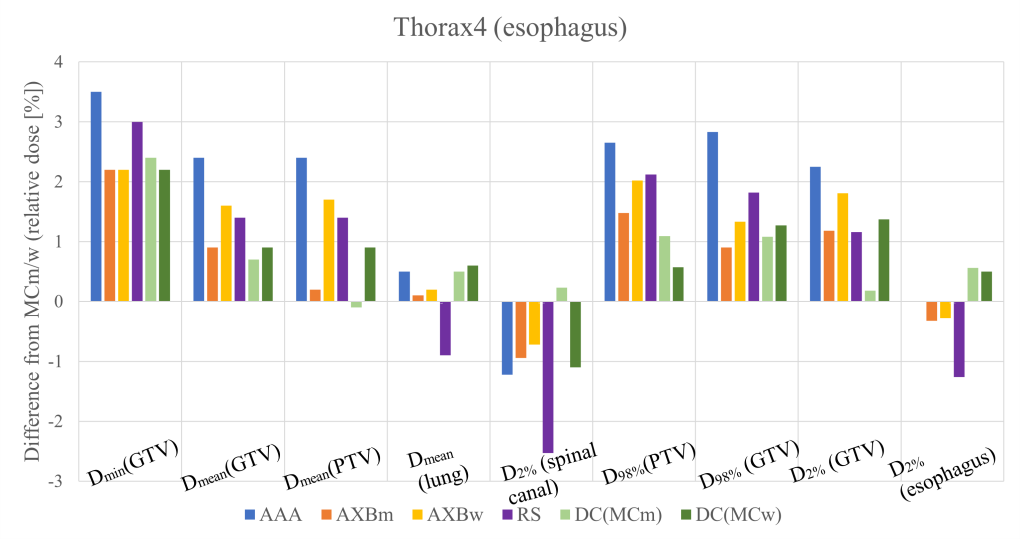

Figure 4.10: A bar plot over the differences between the algorithms AAA, $AXB_{m/w}$, RS, and DC from the MC calculated distribution in plan Esophagus1. Algorithms AAA, AXB_w, and RS are compared to MC_w and AXB_m and DC is compared to MC_m. The differences are calculated in relative dose by subtracting the value of the $MC_{w/m}$ from the value of the respective algorithm.

4.2.5 Overview of the Results

In the above sections algorithm, DC was compared to both MC_m and MC_w. Altogether 60 comparisons between DC and MC were made of which in 38 (63.3%) DC was closer to MC_m than MC_w.

Table 4.2 present the maximum difference, mean difference, the standard deviations,

and a 95% confidence interval for the evaluated algorithms in parameters D_{mean}(PTV) and $D_{98\%}$(PTV). These values are calculated based on all 8 patient plans. The 95% confidence interval was calculated using t-distribution. For parameter D_{mean}(PTV) the calculated 95% confidence interval is within a ±2% difference for algorithms AAA and AXB, and within a ±1.5% difference for AXB_m. Algorithm DC has the biggest 95% confidence interval for parameter D_{mean}(PTV). While algorithm RS has a small interval compared to the other algorithms it has the only interval that does not include 0. This indicates that algorithm RS will in 95% of cases overestimate the dose in D_{mean}(PTV). For parameter $D_{98\%}$(PTV) 95% confidence interval is within a ± 3% difference for all evaluated algorithms.

Table 4.2: Table over the maximum difference, mean different, standard deviation (SD) and 95% confidence interval (CI) in parameters D_{mean}(PTV) and $D_{98\%}$(PTV) for algorithms AAA, $AXB_{m/w}$, RS and DC compared to $MC_{m/w}$. The confidence interval was calculated using the t-distribution.

	Algorithm	**Max [%]**	**Mean [%]**	**SD [%]**	**95% CI [%]**
D_{mean} (PTV)	AAA	2.6	0.89	1.30	[-0.20 1.98]
	AXB_m	-1,4	0.26	1.06	[-0.64 1.49]
	AXB_w	-2,6	0.58	1.43	[-0.62 1.77]
	RS	2.7	1.86	0.71	[1.29 2.46]
	DC	-6,6	-1.03	2.91	[-3.46 1.41]
$D_{98\%}$ (PTV)	AAA	4.19	1.76	1.44	[0.56 2.96]
	AXB_m	2.84	0.97	1.38	[-0.18 2.13]
	AXB_w	3.13	1.26	1.34	[0.15 2.39]
	RS	3.31	2.14	0.74	[1.52 2.75]
	DC	-5.78	-0.90	2.35	[-2.87 1.06]

When recalculating the plans in RS a gamma pass rate was also calculated, the gamma pass rate of the AAA algorithm in each plan is presented in table4.3. The pass rates vary from 64.26% for plan Thorax3(lung) and 99.36% for Thorax4(esophagus). To estimate the general agreement between AAA, $AXB_{m/w}$ and DC the max and mean differences in parameters D_{mean}(PTV) and $D_{98\%}$(PTV) were calculated along with the standard deviation and 95% confidence interval, see table 4.4. These calculations indicate that in 95% cases AAA and $AXB_{m/w}$ will overestimate the dose compared to DC with up to 4.5%.

Table 4.3: Table presenting the gamma pass rate for the AAA algorithms of each plan calculated in RS.

Plan	**DC gamma pass rate [%]**
Prostate1	87.33
Prostate2	78.33
Brain1	71.40
Brain2	94.40
Thorax1 (SBRT)	94.60
Thorax2 (SBRT)	81.48
Thorax3 (lung)	64.26
Thorax4 (esophagus)	99.36
Phantom	99.88

Table 4.4: Table over the maximum difference, mean different, standard deviation (SD) and 95% confidence interval (CI) in parameters D_{mean}(PTV) and $D_{98\%}$(PTV) for algorithms AAA and $AXB_{m/w}$ compared to DC. The confidence interval was calculated using the t-distribution.

	Algorithm	**Max [%]**	**Mean [%]**	**SD [%]**	**95% CI [%]**
D_{mean} (PTV)	AAA	6.6	3.41	0.79	[2.75 4,07]
	AXB_m	5.2	2.19	0.96	[1.39 2.99]
	AXB_w	5.4	3.1	0.96	[2.30 3.90]
$D_{98\%}$ (PTV)	AAA	5.16	3.10	1.09	[2.19 4.01]
	AXB_m	4.14	1.79	1.30	[0.70 2.88]
	AXB_w	4.41	2.60	2.28	[0.69 4.51]

4.3 Discussion

As expected the algorithm AXB_m, the algorithm with the most algorithmic similarities to MC has the best agreement with MC, this underlines the benefits of changing over from AAA to AXB in clinical settings. It was also found that in general DC was in better agreement with MC_m than with MC_w. As discussed in section 2.2.4 the DC algorithm can be seen as dose-to-water within mediums similar to water but more leaning towards dose-to-medium within mediums such as bone and lung tissue. Our results suggest that within patient plans, where bone and lung tissue often is involved, DC's dose presentation is in more agreement with dose-to-medium. Overall DC did underestimate the dose compared to MC and the other algorithms.

RS was in the least agreement with MC. The biggest deviations, overall, from the MC dose distributions are seen in thoracic planes. This is in agreement with the results of the phantom evaluations which suggest that all algorithms differ the most in bone and lung, the thorax plans are the only ones containing both these elements. Especially AAA differed in the lung region in the phantom, which is replicated in plans thorax2 and thorax4, where AAA stands out with big differences. When comparing the results of parameter $D_{98\%}$(PTV) in the prostate plans it was also suggested that the bones in the PTV of plan Prostate2 create an enhanced difference from the MC distribution. It should be noted that AAA's and RS's dose-to-water differ from the dose-to-water calculated by MC, as mentioned in section 2.2, especially in the interface between water like and non-water like material (such as bone)[18]. This may have enhanced the differences, compared to the differences found between AXB_m and MC_m.

The results in this thesis were compared to a previous 6X MC evaluation of AAA calculated patient plans done with the same MC system [17]. The study ref. [17] found that the difference between AAA and MC was within 1.5% for D_{mean}(PTV) and within 3% for parameters such as $D_{95\%}$(PTV), which are more sensitive to the shape of DVH [17]. In this thesis $D_{98\%}$ was used instead of $D_{95\%}$, as it is the one more used in clinical settings.

The 95% confidence interval presented in table 4.2 indicates a similar agreement as was found in study ref. [17], as parameter $D_{98\%}$ was found to differ $< \pm 3\%$ for all algorithms. For parameter D_{mean} the agreement was within 2% for algorithms AAA and AXB but not for RS and CC, which indicates less compliance compared to ref. [17], where AAA 6X plans were evaluated. It should be noted that the ref. [17] did not look at brain plans but prostate, thorax, gynecological and head and neck plans. Altogether the study [17] evaluated 70 patient plans, compared to the 8 patient plans evaluated in this thesis. To more reliably evaluate how the accuracy of 6FFF plans looks compared to 6X plans more plans should be evaluated, but the results in this thesis indicate a good agreement with MC for 6FFF plans calculated with the algorithms AAA and AXB. Aside from evaluating more plans, the evaluations could be made more rigorous by also using a gamma evaluation. This was considered during the lapse of the thesis but as the DICOM format of the MC distributions did not import to the gamma evaluation tool available, it was not done.

The results of this thesis suggest that algorithms AAA and AXB do create accurate plans for energy 6FFF. These results should continue to be evaluated to further implement the use of 6FFF plans in a clinical setting when appropriate. The results also suggest that a possible calibration of DC is needed before it is used as QA for 6FFF plans.

5

Summery and Conclusions

This thesis aimed to evaluate static and dynamic 6FFF dose distributions calculated with AAA, AXB, RS and DC against MC-data. Based on the results presented in section 4.2 it can be concluded that Eclipse algorithms AAA and AXB agree within 2% for parameter D_{mean}(PTV) and 3% $D_{98\%}$(PTV) with MC. These results indicate that no notable loss in accuracy is caused by using 6FFF compared to 6X, as a similar agreement for AAA was found in a previous study [17] evaluating 6X distributions. The results also suggest that the CC implementations in DC and RS have less agreement with MC for 6FFF compared to the Eclipse algorithms.

The underestimation of the dose calculated by DC seen in the water phantom, chapter 3, was also observed in patient plans, chapter 4, suggesting that something in the beam model needs to be calibrated to better agree with MC calculations. The larger differences between MC and RS in patient plans were more unexpected, as RC did not differ from MC in the water phantom as notable as DC. This suggests that something specific to the patient plans is the cause for these differences, as opposed to the beam model. A likely origin for the differences is the MLC modeling. While the number of plans evaluated limits the generalizability of the results it gives a good indication of the accuracy of the algorithms for different cancer sites. Based on these results further investigations of RS and DC should be performed before clinical use. As DC was found to constantly underestimate the dose, proposing this can be fixed by calibrating the DCs 6FFF beam model with measured data.

The methods used to validate the MC 6FFF presented in this thesis were considered sufficient and exact calibration of the MC system was achieved. Both the one-field water phantom evaluation and the one-field lung phantom evaluation of the algorithms were helpful as they provided context to the following patient plan evaluations.

Based on the results presented in this thesis, it would be of interest to continue evaluating FFF plans with MC to verify the accuracy demonstrated. It is also of interest to evaluate more cancer sites, such as treatments in the head and neck area. Investigating possibilities of modifying the MC system so that SRS plans can also be evaluated is also of interest because a reduction of treatment time is especially interesting for treatments with high doses.

Bibliography

[1] M. Dalaryd, "Dosimetric effects of removing the flattening filter in radiotherapy treatment units," English, Ph.D. dissertation, Medical Radiation Physics, Lund, 2015.

[2] R. Ottosson, "Monte carlo treatment planning for advanced radiotherapy," English, Ph.D. dissertation, DTU nutech, 2015.

[3] S. Aoki, H. Yamashita, A. Haga, *et al.*, "Flattening filter-free technique in volumetric modulated arc therapy for lung stereotactic body radiotherapy: A clinical comparison with the flattening filter technique.," *Oncology Letters*, vol. 153, pp. 3928–3936, 2018.

[4] T. Ji, L. Sun, F. Cai, and G. Li, "Comparison between flattening filter-free (fff) and flattened photon beam vmat plans for the whole brain radiotherapy (wbrt) with hippocampus sparing," *Asia-Pacific Journal of Clinical Oncology*, vol. 18, no. 5, e263–e267, 2022.

[5] M. Ahlström, "Flattening filter free volumetric modulated arc therapy for extreme hypo-fractionation of prostate cancer- decreasing the treatment time and reducing the impact of prostate motion," Master Thesis, Lund University, 2015.

[6] International Atomic Energy Agency, *History of radiotherapy – a short introduction*, Accessed Dec. 16, 2022. [Online]. Available: `https://humanhealth.iaea.org/HHW/MedicalPhysics/Radiotherapy/Topicsofspecialinterest/HistRT/index.html`.

[7] P. Metcalfe, T. Korn, and P. Hoban, *The Physics of Radiotherapy X-Ray and Electrons*, 1st ed. Madison: Medical Physics Publishing, 2007.

[8] S. Jiang, G. Sharp, T. Neicu, R. Berbeco, S. Flampouri, and T. Bortfeld, "On dose distribution comparison," *Physics in Medicine and Biology*, vol. 51, pp. 759–776, 2006.

[9] S. F. Kry, V. Feygelman, P. Balter, *et al.*, "Aapm task group 329: Reference dose specification for dose calculations: Dose-to-water or dose-to-muscle?" *Medical Physics*, vol. 47, no. 3, e52–e64, 2020.

[10] M. Fippel, "Basics of monte carlo simulations," in *Monte Carlo Techniques in Radiation Therapy*, J. Seco and F. Verhaegen, Eds., 1st ed., CRC Press, 2013, ch. 2, pp. 17–28.

[11] M. J. Berger, "Monte Carlo Calculation of the penetration and diffusion of fast charged particles," *Methods in Comput. Phys.*, vol. 1, pp. 135–215, 1963.

[12] I. Kawrakow, E. Mainegra-Hing, D. Rogers, F. Tessier, and B. Walters, *The egsnrc code system: Monte carlo simulation of electron and photon transport*, National Research Council Canada, Ottawa, Canada, 2018.

[13] J. Sievinen, W. Ulmer, and W. Kaissl, "Aaa photon dose calculation model in eclipse," Varian Medical Systems, Tech. Rep. 7170A, 2013.

[14] V. Löf, "The difference between a collapsed cone based and a monte carlo based dose calculation algorithm," Master Thesis, KTH School of Engineering Sciences, 2015.

[15] SunNuclear, *Dosecheck perfraction*, SunNucelar corporation, Melbourne USA, 2015. [Online]. Available: `https://www.sunnuclear.com/uploads/documents/whitepapers/DC_PF_Accuracy-of-the-SNC-Dose-Calculator_091216.pdf`.

[16] A. Fogliata, G. Nicolini, A. Clivio, E. Vanetti, and L. Cozzi, "Dosimetric evaluation of acuros xb advanced dose calculation algorithm in heterogeneous media," *Radiation Oncology*, vol. 6:82, p. 82, 2011.

[17] R. Chakarova, R. Cronholm, M. Krantz, P. Andersson, and A. Hallqvist, *2018:01 monte carlo patient-specific pre-treatment qa system for volumetric modulated arc therapy*, Strålsäkerhets Myndigheten, 2018. [Online]. Available: `https://www.stralsakerhetsmyndigheten.se/en/publications/reports/radiation-protection/2018/201801/`.

[18] N. Reynaert, F. Crop, E. Sterpin, I. Kawrakow, and H. Palmans, "On the conversion of dose to bone to dose to water in radiotherapy treatment planning systems," *Physics and Imaging in Radiation Oncology*, vol. 5, pp. 26–30, 2018.

A

Appendix

A.1 Extended results

The dose distributions calculated with DoseCheck was compared to AAA in a water phantom, field size 20x20 cm^2, a profile at depth 100 mm. The results are presented in the figure A.1.

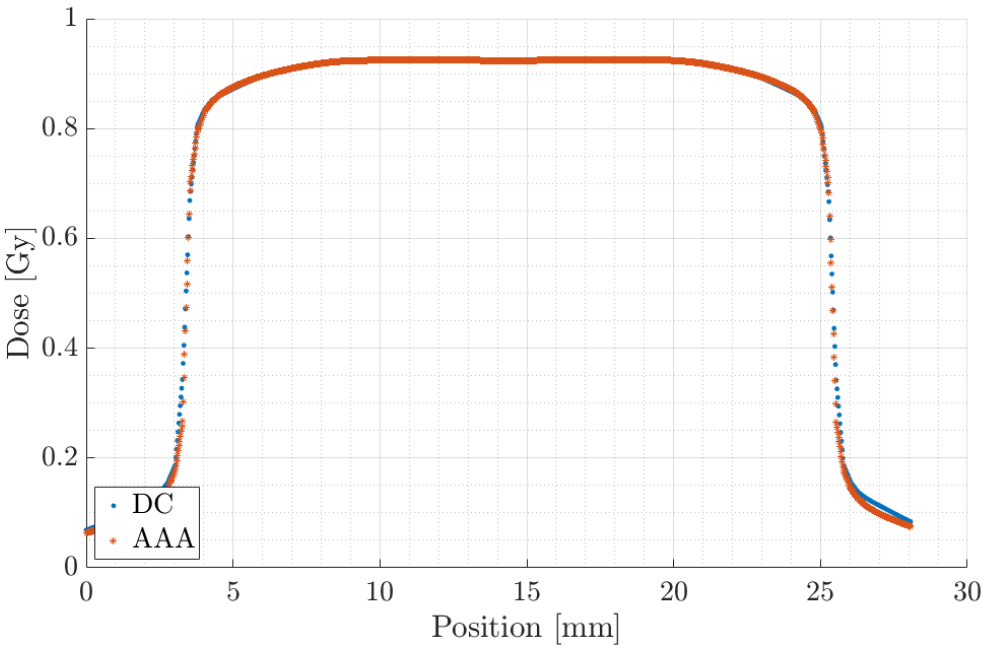

Figure A.1: Figure presenting the DC and AAA profiles at depth 100 mm and with field size 20x20 cm^2.